Thermal analysis of finite length journal bearings including fluid inertia

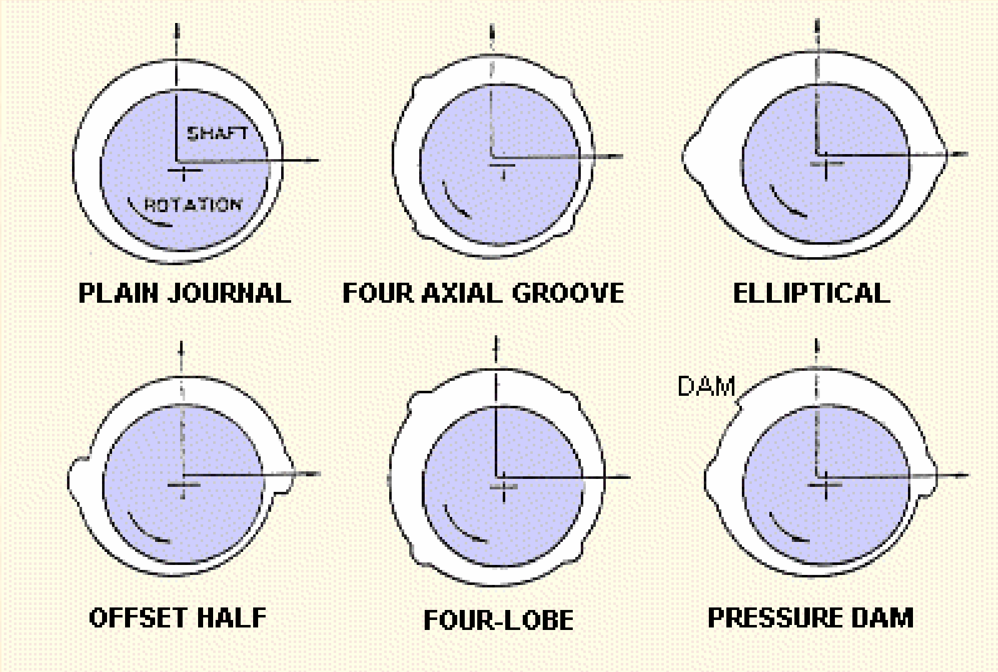

Luis San Andres
Mast-Childs Professor
Sept 2009

NOTES 7

THERMAL ANALYSIS OF FINITE LENGTH JOURNAL BEARINGS INCLUDING FLUID INERTIA EFFECTS

Notes 4 and 5 presented the derivation of the pressure field, load capacity and dynamic force coefficients in a short length cylindrical journal bearing. Notes 7 present an analysis for the prediction, using numerical methods, of the static load capacity and dynamic force coefficients in finite-length journal bearings. Practical bearing geometries include lubricant feeding arrangements (grooves and holes), multiple pads with mechanical preloads to enhance their load capacity and stability. The analysis includes the evaluation of the film mean temperature field from an energy transport equation. The film temperature affects the viscosity of the lubricant within the fluid flow region. In addition, the analysis includes temporal fluid inertia effects modifying the classical Reynolds equation; and hence, the model predicts not only stiffness and damping force coefficients but also added mass coefficients. As recent test data shows, fluid inertia effects cannot longer be ignored in journal bearing forced performance, static or dynamic.

Introduction

Analysis of the dynamic performance of rotors supported on fluid film bearings relies not just on the rotor structural (mass and elastic) properties but also on the acurate evaluation of the static and dynamic forced performance characteristics of the bearing supports. A rotordynamic analysis delivers synchronous response to imbalance and stability results in accordance with API requirements, to demonstrate certain performance characteristics ; and on occasion, to reproduce peculiar field phenomena and to troubleshoot malfunctions or limitations of the operating system.

Mineral-oil lubricated bearings support most commercial machinery that operate at low to moderately high rotational shaft speeds. The bearings carry heavy static loads, mainly a fraction of the rotor weight. The lubricant, supplied from an external reservoir, fills the small clearance separating the shaft (journal) from the bearing. Shaft rotation drags the lubricant through the bearing film lands to form the hydrodynamic wedge that generates the hydrodynamic fluid film pressure that, acting on the journal, is able to support or carry the applied static load. The mineral oil lubricant, generally of large viscosity, increases its temperature as it carries away the mechanical energy dissipated into heat. Hence, the material visosity of the lubricant, a strong function of temperature, does not remain constant within the film flow region in the bearing.

Importantly enough, the conditions of low speed (Ω), small clarance *(c)*, and large viscosity (μ/ρ) determine a laminar flow condition in the bearing, i.e. operation with small Reynolds numbers Re < 1,000 ($Re=\rho\Omega Rc/\mu$). Hence, Reynolds equation of Classical Lubrication is valid for prediction of the equilibrium hydrodynamic film pressure in the bearing. The prediction of the thermal energy transport in a thin film bearing is more difficult since there is a significant temperature along and accross the film, i.e. a three-dimensional phenomenon. Most importantly, the thermal energy exchange does not just involve the mechanical energy generated by shear and its advection by the lubricant flow but also must account for the heat conduction into or from the shaft and bearing cartridge.

A comprehensive 3-D thermohydrodynamic analysis for prediction of performance in finite length journal bearings is out of the scope of these lecture notes. The interested reader should refer to relevant work in the archival literature [1,2] for further details. However, note that most fluid film bearing designers and bearing manufacturers rarely rely on cumbersome and computationally expensive analysis tools; in particular when these require of boundary conditions that are operating system dependent (not general). More than often, engineers prefer to obtain model results that are in agreement with published test data and go along with their vast practical experience.

Analysis

Figures 1 and 2 depict the geometry of typical cylindrical journal bearings comprised of a journal rotating with angular speed (Ω) and a bearing with one or more arcuate pads. A film of lubricant fills the gap between the bearing and its journal. Journal center dislacements (e_X, e_Y) refer to the (X,Y) inertial coordinate system. The angle Θ, whose origin is at the $-X$ axis, aids to describe the film geometry. The graphs show the relevant nomenclature for analysis.

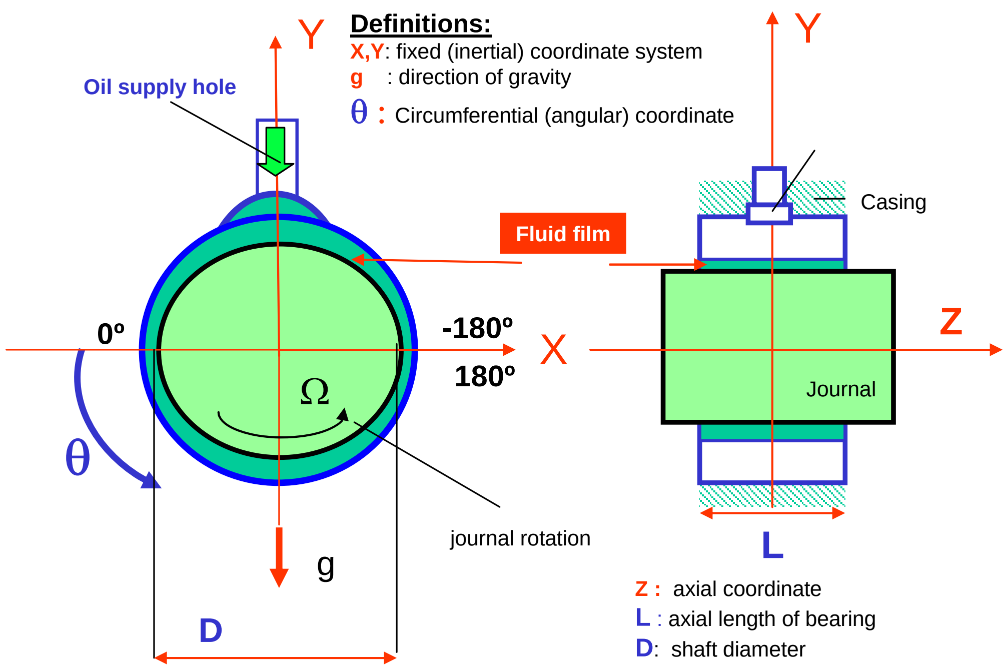

Figure 1. Geometry of a cylindrical bearing pad with feed hole (not to scale)

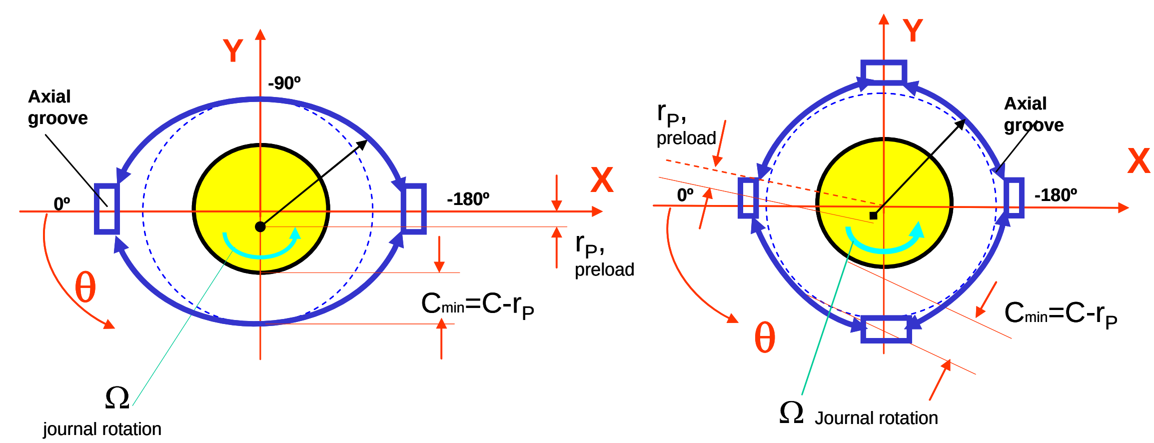

Figure 2. Geometry of elliptical (two groove) and four-pad cylindrical bearings (not to scale)

Figure 3 shows a typical bearing pad with radial clearance (*c)* and preload (r_P) at angle Θ_P. Θ_l and Θ_t denote the leading edge and trailing edges of the pad, respectively. Within the flow region $\{\Theta_l \le \Theta \le \Theta_t,\ 0 < z < L\}$, the film thickness *(h)* is

$$h = c - r_p \cos(\Theta - \Theta_p) + e_{X(t)} \cos\Theta + e_{Y(t)} \sin\Theta \tag{1}$$

where $(e_X, e_Y)_{(t)}$ are the journal center eccentricity components along the (*X, Y*) directions.

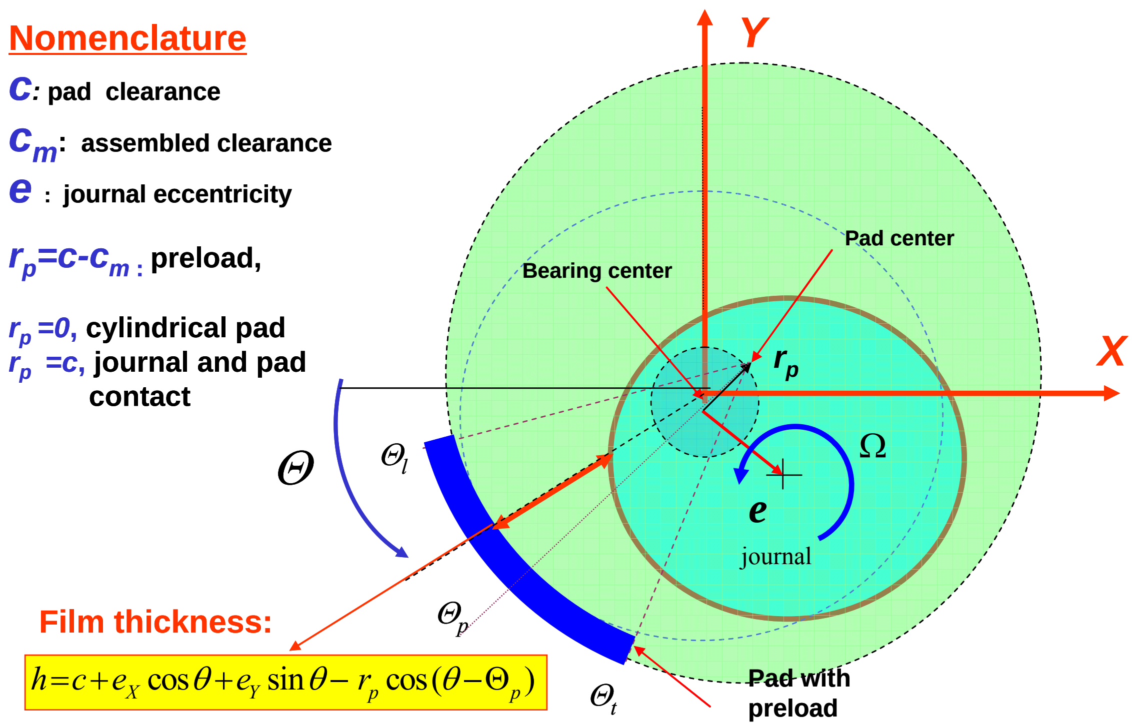

Figure 3. Geometry of a bearing pad with preload and description of film thickness (not to scale)

Governing equations for pressure generation and temperature transport

The modified [3,4,5] laminar flow Reynolds equation describing the generation of hydrodynamic pressure (*P*) in the thin film region $\{\Theta_l \le \Theta \le \Theta_t,\ 0 < z < L\}$ of a bearing pad is

$$\frac{1}{R^2}\frac{\partial}{\partial \Theta}\left(\frac{h^3}{12\,\mu_{(T)}}\frac{\partial P}{\partial \Theta}\right) + \frac{\partial}{\partial z}\left(\frac{h^3}{12\,\mu_{(T)}}\frac{\partial P}{\partial z}\right) = \frac{\partial h}{\partial t} + \frac{\Omega}{2}\frac{\partial h}{\partial \Theta} + \left(\frac{\rho h^2}{12\,\mu_{(T)}}\right)\frac{\partial^2 h}{\partial t^2} \tag{2}$$

Geometry for bearing pad with preload

Nomenclature

c: pad clearance

c_m: assembled clearance

e : journal eccentricity

$r_p = c - c_m$: preload,

$r_p = 0$, cylindrical pad
$r_p = c$, journal and pad contact

Note: angle Θ origin starts from -X axis

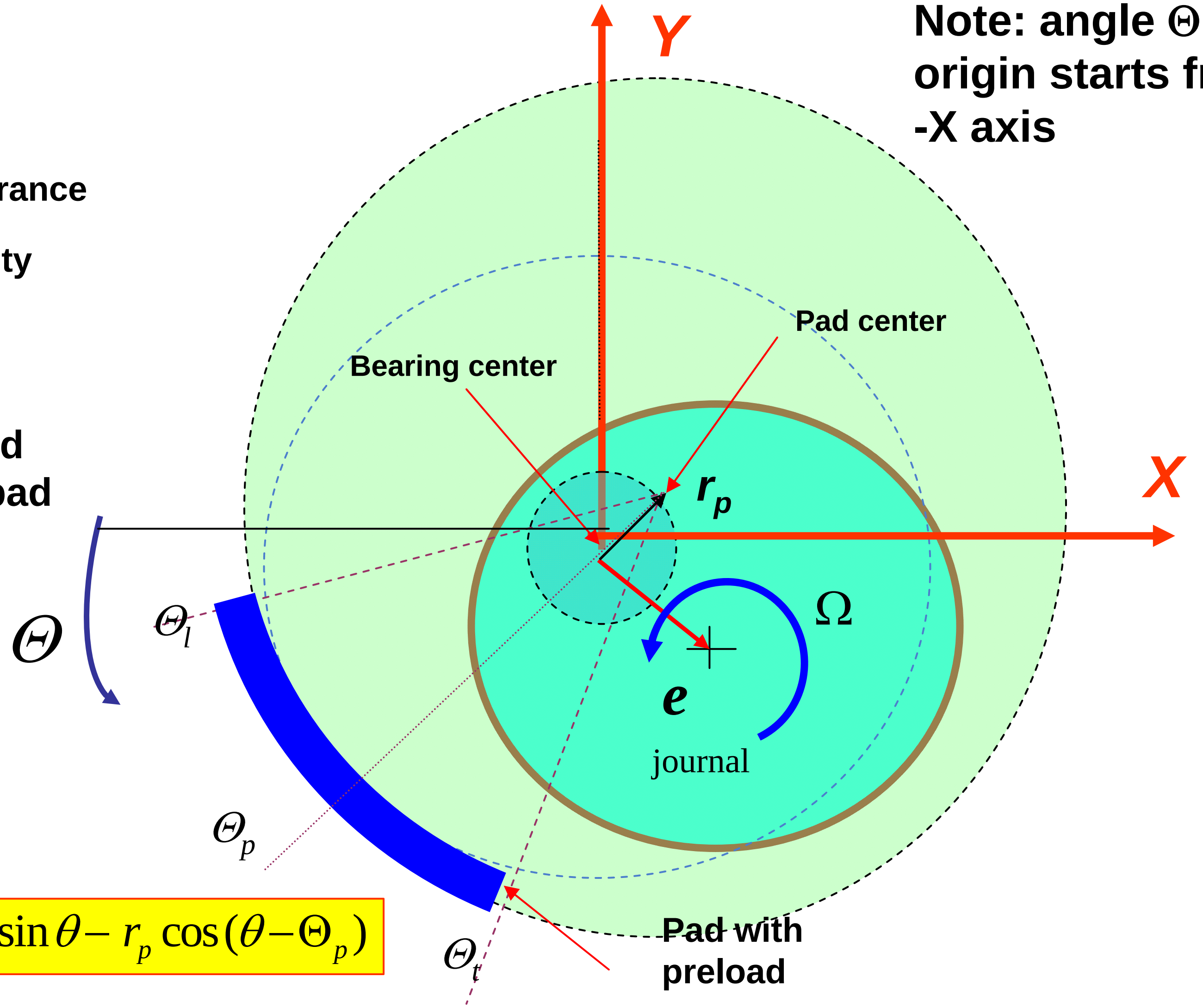

Film thickness:

$$h = c + e_X \cos\theta + e_Y \sin\theta - r_p \cos(\theta - \Theta_p)$$

Ask about:

What is a pad preload?

What is the pad offset?

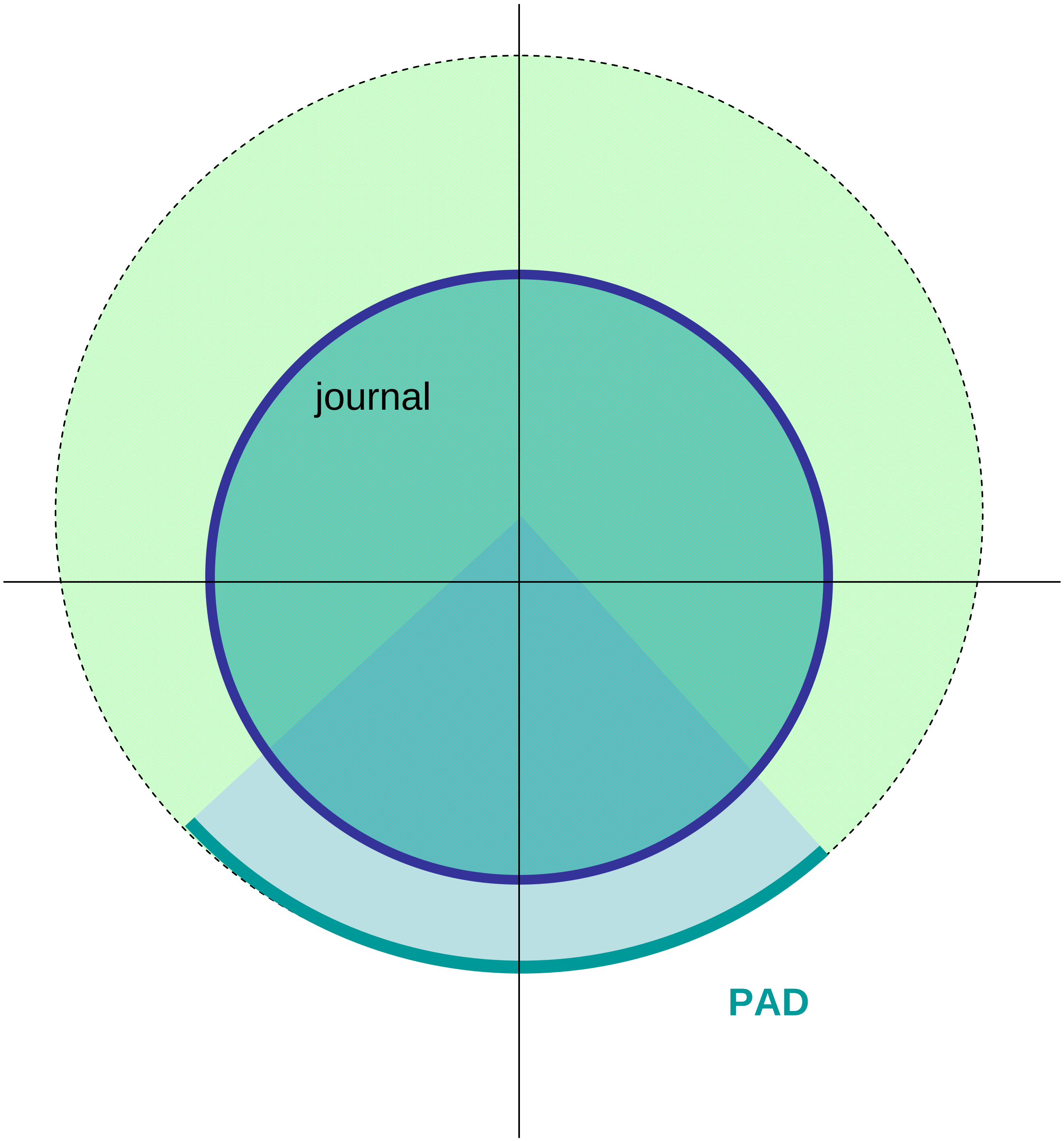
journal
PAD

OFFSET = 50%

Positive preload

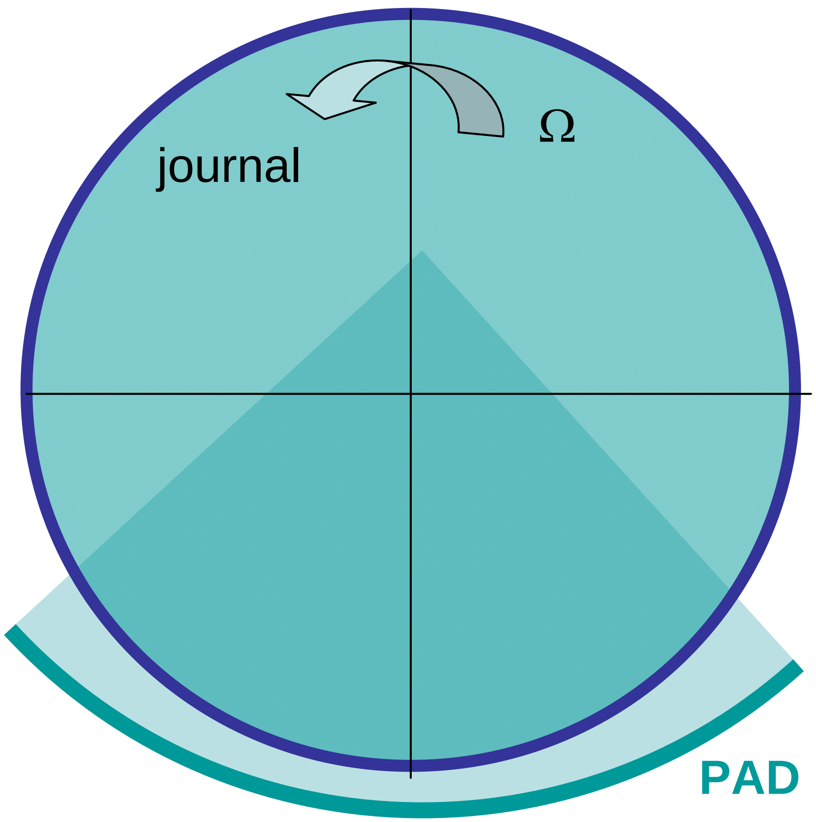

Zero preload

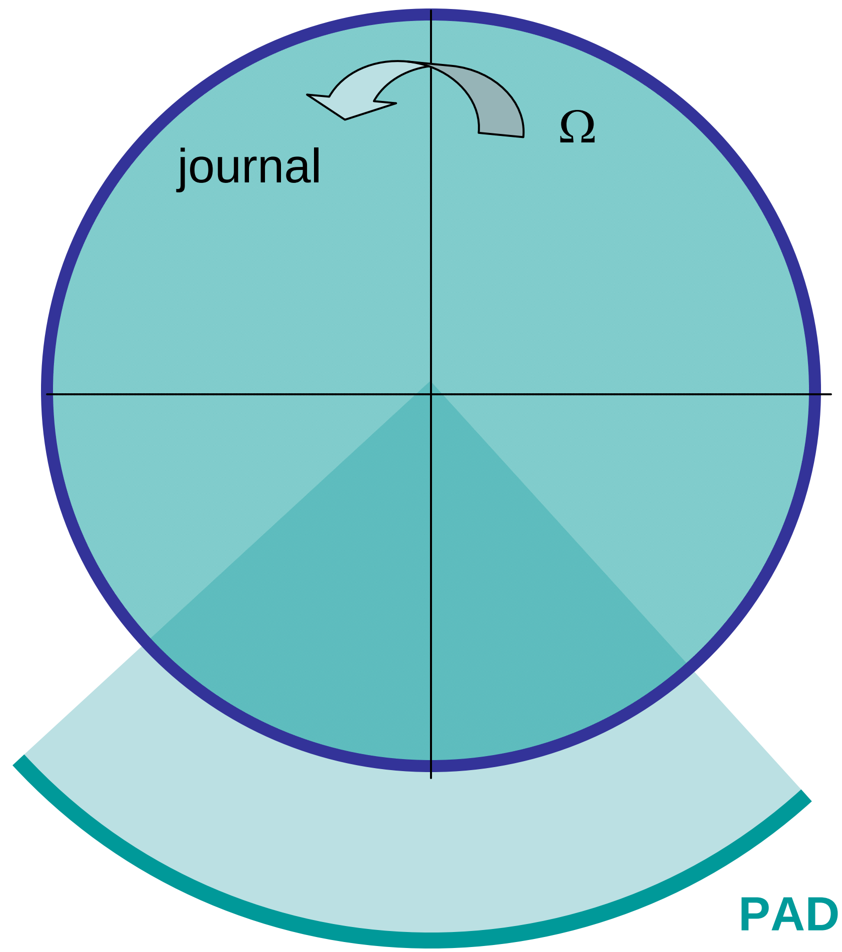

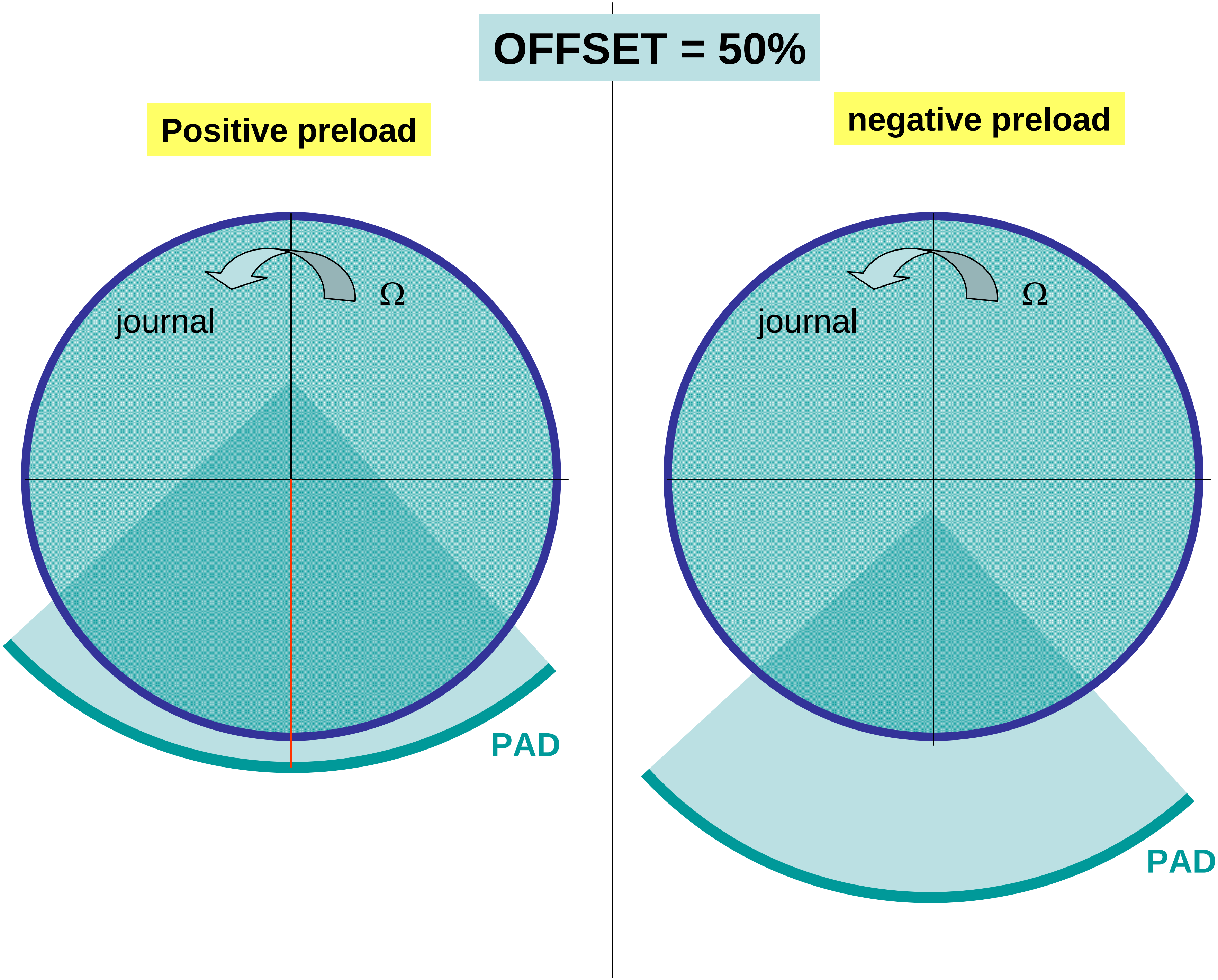
OFFSET = 50%
Positive preload
negative preload
journal
Ω
journal
Ω
PAD
PAD

OFFSET = 50%

Positive preload

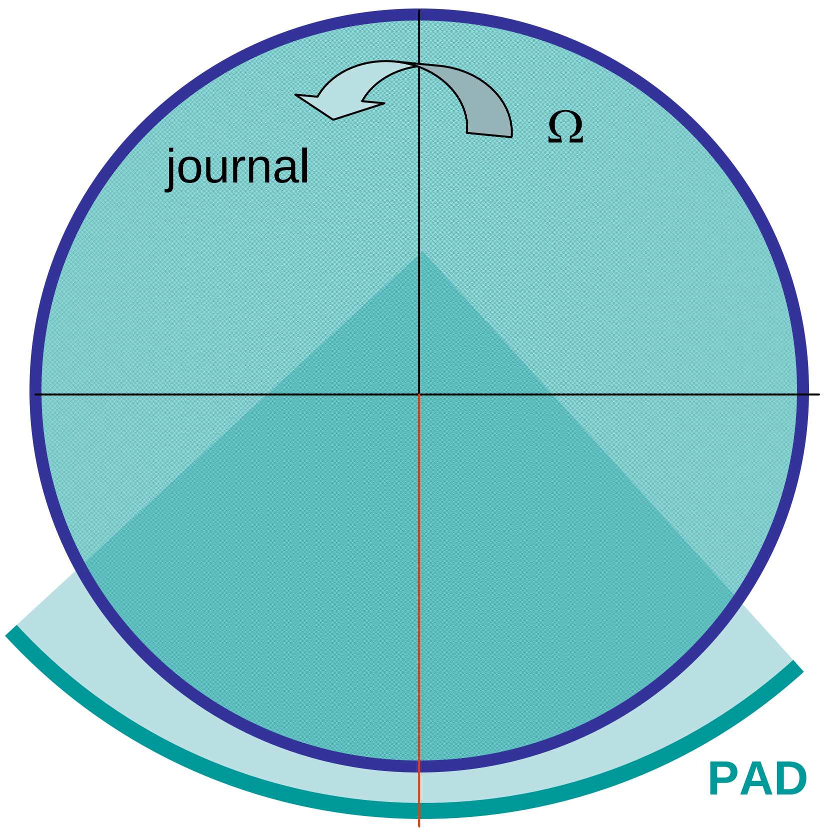

OFFSET ~ 75 %

Positive preload

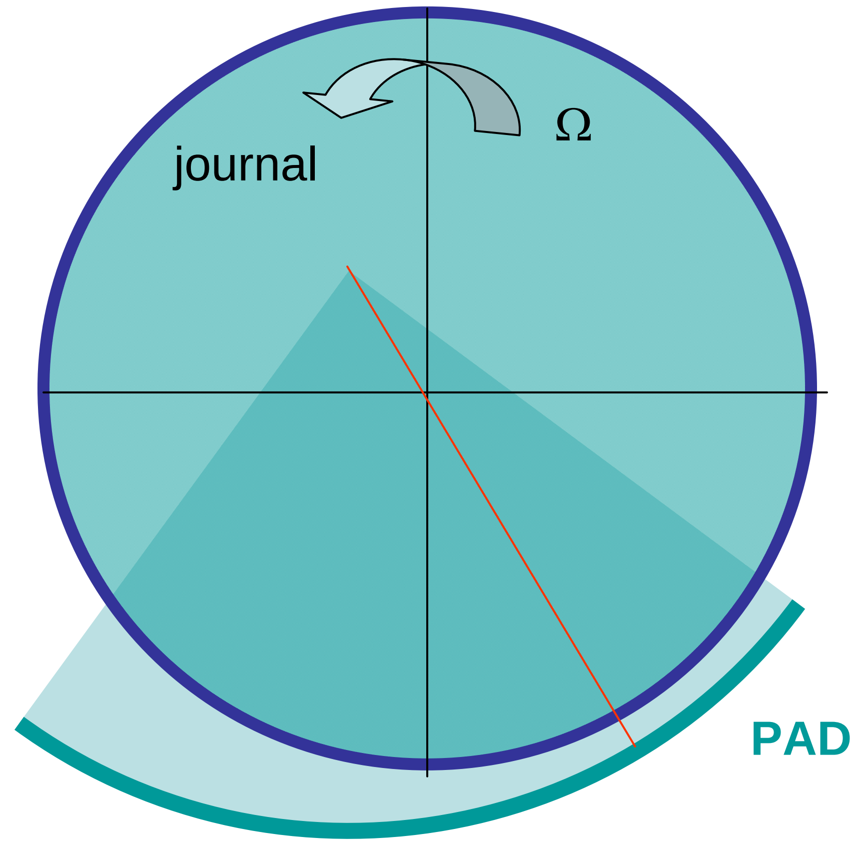

OFFSET = 50%

Positive preload

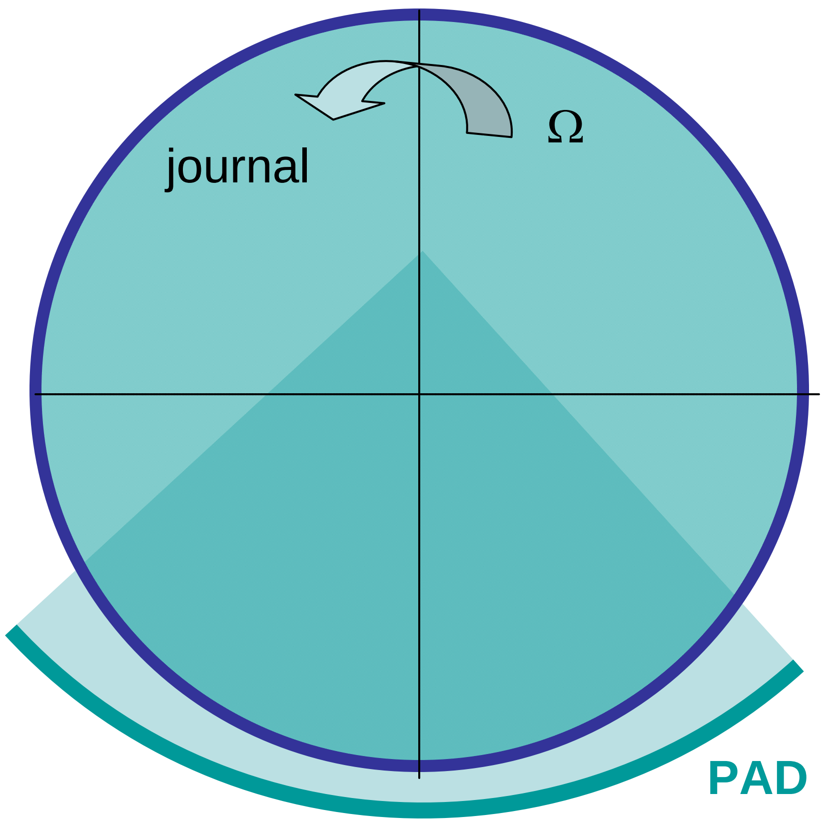

OFFSET ~ 25 %

Positive preload

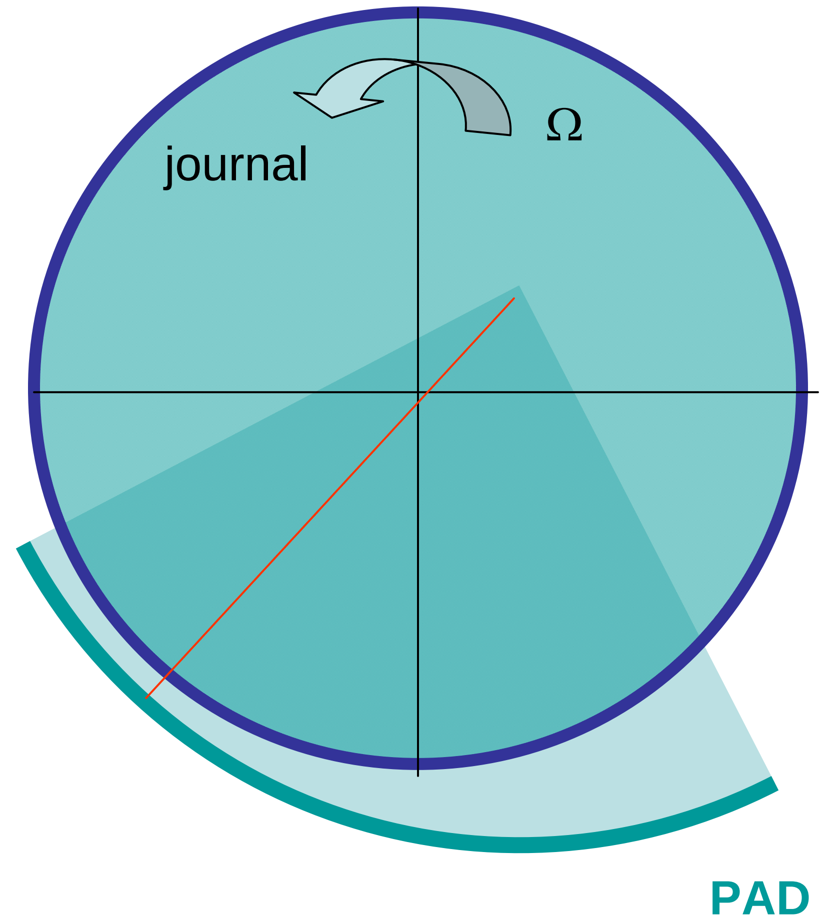

where (ρ, μ) denote the lubricant density and viscosity, both temperature (T) dependent material properties. For example, $\mu = \mu_S \, e^{-\alpha_v (T - T_S)}$, with subindex S denoting supply conditions. The modified Reynolds equation includes temporal fluid inertia effects ; hence, the flow model is strictly applicable to lubricant thin film flows induced by small amplitude journal motions about an equilibrium position.

For the laminar flow of an incompressible fluid and regarding the temperature as uniform along the axial direction, the energy transport equation under steady-state conditions is [6]

$$C_v \left[\frac{\partial}{R \partial \Theta} \left(\rho h U T \right) + \frac{\partial}{\partial z} \left(\rho h W T \right) \right] + Q_s = S = \frac{12 \mu}{h} \left(W^2 + \frac{\Omega^2 R^2}{12} + \left[U - \frac{\Omega R}{2} \right]^2 \right) \quad (3)$$

where T is the lubricant bulk-temperature[1] and $Q_s = \bar{h}_B \left(T - T_B \right) + \bar{h}_J \left(T - T_J \right)$ is the heat flow into the bearing and journal surfaces. Above, C_v is the lubricant specific heat, and *(W, U)* represent the axial and circumferential mean flow velocities given by

$$W = -\frac{h^2}{12 \mu} \frac{\partial P}{\partial z}; \;\; U = -\frac{h^2}{12 \mu} \frac{\partial P}{R \partial \Theta} + \frac{\Omega R}{2} \quad (4)$$

Eq. (3) is representative of a bulk-flow model that balances the mechanical shear dissipation energy (*S)* to the thermal energy transport due to advection by the fluid flow and convection (Q_s) into the bearing surfaces. The heat convection coefficients $\left(\bar{h}_B, \bar{h}_J \right)$ depend on the Prandtl number ($P_r = C_v \, {}^{\mu}\!/_{\kappa}$) and the flow condition defined by the local Reynolds number $\left(R_e = \frac{\rho U h}{\mu} \right)$ relative to the bearing and journal surfaces[7]. For laminar flow, $R_e \frac{c}{R} \le 1$, Colburn's analogy renders the convection coefficients $\bar{h} = 3 P_r^{1/3} \frac{\kappa}{h}$. See Ref. [8] for details[2].

---

[1] The bulk temperature represents an average across the film thickness, i.e. $T = \frac{1}{h} \int_0^h T_{(\Theta, z, y)} \, dy$

[2] The THD model implements a number of heat transfer models, including those for fixed or developing wall temperatures and heat flows.

Boundary conditions for film pressure and temperature[3]

The pressure at a pad leading edge equals a supply condition, i.e.

$$0 \le z \le L : P\left(\Theta_l, z\right) = P_S \tag{5a}$$

The pressure is ambient at the bearing axial ends,

$$\Theta_l \le \Theta \le \Theta_t : P(\Theta, 0) = P_a ; \quad P(\Theta, L) = P_a ; \tag{5b}$$

and also at the pad trailing edge,

$$0 \le z \le L : P\left(\Theta_t, z\right) = P_a \tag{5c}$$

Furthermore, within the whole flow domain, $P > P_{cav}$, i.e., the film pressure must be higher than the lubricant cavitation pressure. For a thorough discussion on lubricant cavitation and physical sound boundary conditions refer to Notes 6 [9].

Lubricant is supplied into the bearing at a known supply temperature (T_S). The fluid temperature *(T)* gradually increases as it flows through the film thickness in a bearing pad since the lubricant removes shear induced mechanical energy. At the leading edge of a pad (Θ_l), there is mixing of the supplied cold lubricant flow rate (F_S) and a fraction of the hot lubricant flow (F_{up}) leaving the upstream with temperature T_{up}. The flow and thermal energy mixing conditions, as shown in schematic form in Figure 4, are specified as

$$\begin{gathered} F_{in} = F_S + \lambda F_{up} \\ C_v \left(F_{in} T_{in} = F_S T_S + \lambda F_{up} T_{up} \right) \end{gathered} \tag{6}$$

where $F_{in} = \int_0^L \left(\rho W h\right)\Big|_{\Theta_l} dz$ is the volumetric flow rate entering the pad at temperature T_{in}, and $F_{up} = \int_0^L \left(\rho W h\right)\Big|_{\Theta_t} dz$. The mixing parameter $\lambda\left(\in[0,1]\right)$ is an empirical variable. Current or modern oil feed flow configurations incorporate direct impingement of the lubricant into a bearing pad, thus λ is low, to render cool lubricant temperature operation, i.e. $T_{in} \sim T_S$. In general, $\lambda \sim$ 0.6-0.9 [10] for conventional feed arrangements with deep grooves and wide holes. In addition, note that the mixing thermal coefficient tends to increase $\left(\lambda \to 1\right)$ with journal speed.

---

3 In a symmetric and aligned bearing, the pressure field is symmetric about the bearing mid axial plane. Thus, only the pressure field for one-half bearing length needs be calculated, say from $z = ½ L$ to $z=L$. In this case, $\left(\partial P / \partial z\right) = 0$ at $z = ½ L$.

That is, as the operating speed increases it becomes increasingly difficult to suminister fresh or cold lubricant into the fluid film bearing.

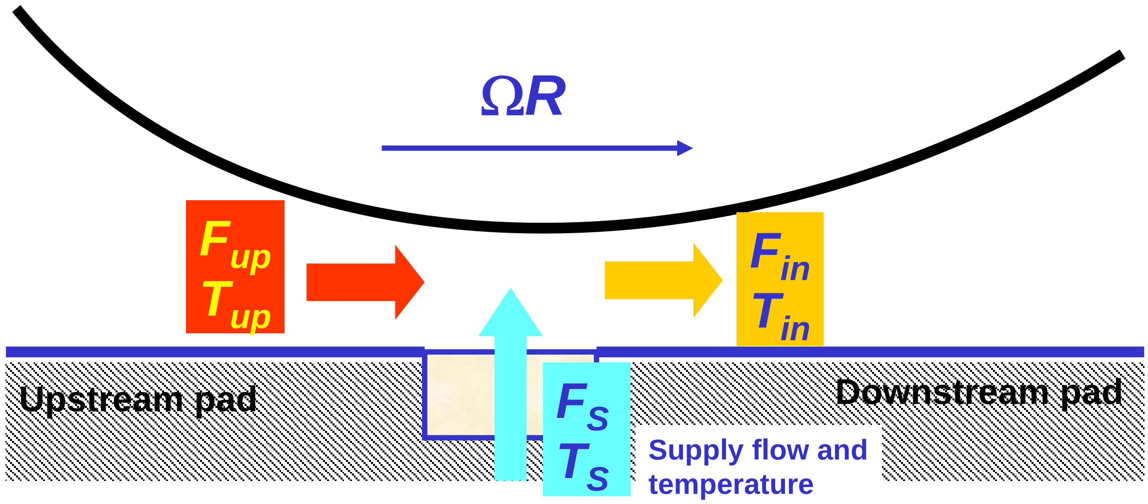

Figure 4. Schematic view of thermal mixing at the leading edge of a bearing pad (*F*: flow, *T*: temperature)

Since the thermal energy transport Eq. (3) is parabolic, there is no need to specify any other temperature along the other pad boundaries. Solution of Eq. (3) determines the lubricant temperature exiting a bearing pad through its axial sides ($z=0, L$) and at the pad trailing edge (Θ_t). Importantly enough, in the region where the lubricant cavitates ($P=P_{cav}$), the (current) analysis assumes there is no further generation of mechanical energy; and consequently, the fluid temperature in this region is constant. This is not an oversimplification, as verified by predictive analysis [11] and various published measurements,see [12,13].

Perturbation analysis[4]

Consider journal center motions of small amplitude ($\Delta X, \Delta Y << c$) about a static equilibrium position $\left(e_{X_0}, e_{Y_0}\right)$, as shown in Figure 5.

$$e_X = e_{X_0} + \Delta X_{(t)},\ \ e_Y = e_{Y_0} + \Delta Y_{(t)} \tag{7}$$

4 Follows the classical analysis of J.W. Lund in Refs. [14,15]

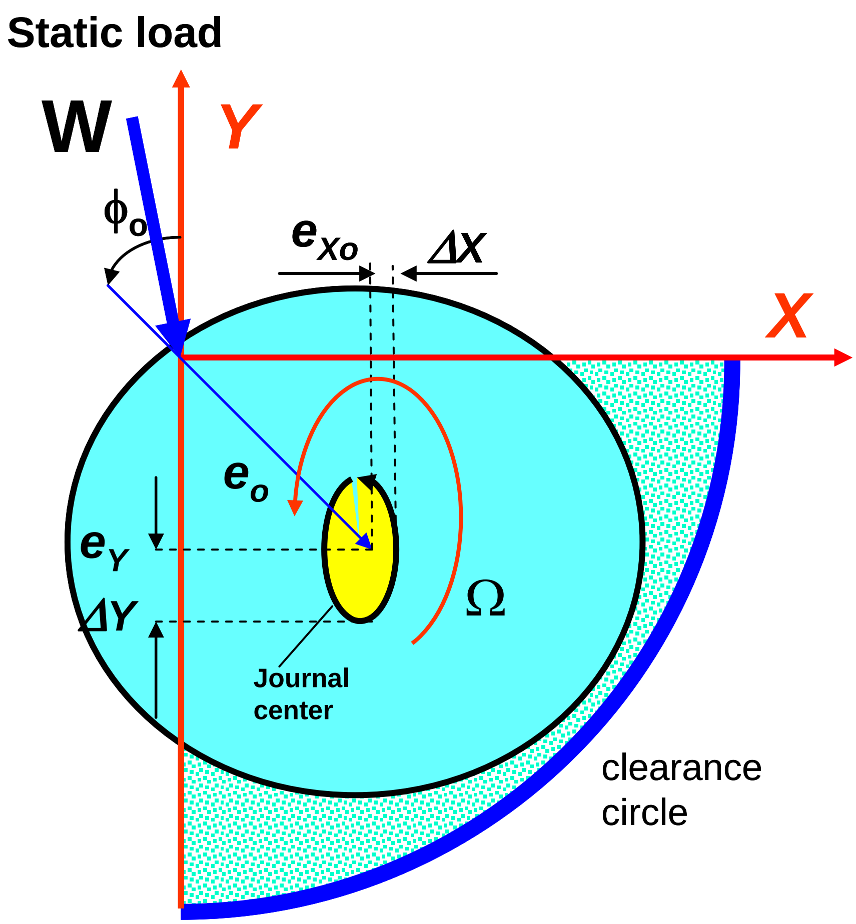

Figure 5. Depiction of small amplitude journal motions about an equilibrium position (Not to scale).

The film thickness is expressed as the superposition of an equilibrium (*zeroth-order*) thickness (h_0) and a *first-order* thickness (Δh_1), i.e.

$$h = h_0 + \Delta h_{1(t)},$$

$$h_0 = c - r_p \cos(\Theta - \Theta_p) + e_{X_0} \cos\Theta + e_{Y_0} \sin\Theta, \tag{8}$$

$$\Delta h_1 = \Delta X_{(t)} \cos\Theta + \Delta Y_{(t)} \sin\Theta,$$

with

$$\frac{\partial h_0}{\partial \Theta} = +r_p \sin(\Theta - \Theta_p) - e_{X_0} \sin\Theta + e_{Y_0} \cos\Theta; \quad \frac{\partial \Delta h_1}{\partial \Theta} = -\Delta X_{(t)} \sin\Theta + \Delta Y_{(t)} \cos\Theta$$

$$\frac{\partial h}{\partial t} = \Delta \dot{X} \cos\Theta + \Delta \dot{Y} \sin\Theta, \quad \frac{\partial^2 h}{\partial t^2} = \Delta \ddot{X} \cos\Theta + \Delta \ddot{Y} \sin\Theta \tag{9}$$

The perturbation in film thickness leads naturally to a perturbation in film pressure, i.e.

$$P(\Theta,z,t)=P_0(\Theta,z)+\Delta P_1(\Theta,z,t),$$
$$\Delta P_1=P_X\Delta X+P_Y\Delta Y+P_{\dot X}\Delta\dot X+P_{\dot Y}\Delta\dot Y+P_{\ddot X}\Delta\ddot X+P_{\ddot Y}\Delta\ddot Y \tag{10}$$

where P_0 is the *zeroth-order* or equilibrium pressure field defined by $\left(e_{X_0},e_{Y_0}\right)$ at steady operating conditions, and ΔP_1 is the perturbed dynamic pressure field[5].

Define the linear operator

$$\mathsf{L}\left[()\right]=\frac{1}{R}\frac{\partial}{\partial\Theta}\left(\frac{h_0^3}{12\,\mu}\frac{\partial\left[()\right]}{R\,\partial\Theta}\right)+\frac{\partial}{\partial z}\left(\frac{h_0^3}{12\,\mu}\frac{\partial\left[()\right]}{\partial z}\right) \tag{11}$$

Substitution of the pressure (P) and film thickness (h) into the modified Reynolds Eq. (2) gives the following equations for determination of the equilibrium and first order pressure fields

$$\mathsf{L}(P_0)=\frac{1}{R^2}\frac{\partial}{\partial\Theta}\left(\frac{h_0^3}{12\,\mu}\frac{\partial P_0}{\partial\Theta}\right)+\frac{\partial}{\partial z}\left(\frac{h_0^3}{12\,\mu}\frac{\partial P_0}{\partial z}\right)=\frac{\Omega R}{2}\frac{\partial h_0}{R\,\partial\Theta} \tag{12a}$$

$$\mathsf{L}\left(P_X\right)=\frac{\partial}{R\,\partial\Theta}\left\{\cos\Theta\left[\frac{\Omega R}{2}-\frac{3h_0^2}{12\mu}\frac{\partial P_0}{R\,\partial\Theta}\right]\right\}-\frac{\partial}{\partial z}\left\{\frac{3h_0^2}{12\mu}\cos\Theta\frac{\partial P_0}{\partial z}\right\}$$
$$\mathsf{L}\left(P_Y\right)=\frac{\partial}{R\,\partial\Theta}\left\{\sin\Theta\left[\frac{\Omega R}{2}-\frac{3h_0^2}{12\mu}\frac{\partial P_0}{R\,\partial\Theta}\right]\right\}-\frac{\partial}{\partial z}\left\{\frac{3h_0^2}{12\mu}\sin\Theta\frac{\partial P_0}{\partial z}\right\} \tag{12b}$$

$$\mathsf{L}\left(P_{\dot X}\right)=\cos\Theta;\qquad \mathsf{L}\left(P_{\dot Y}\right)=\sin\Theta \tag{12c}$$

$$\mathsf{L}\left(P_{\ddot X}\right)=\left(\frac{\rho h_0^2}{12\mu}\right)\cos\Theta;\qquad \mathsf{L}\left(P_{\ddot Y}\right)=\left(\frac{\rho h_0^2}{12\mu}\right)\sin\Theta \tag{12d}$$

where $h_0=c-r_p\cos(\Theta-\Theta_p)+e_{X_0}\cos\Theta+e_{Y_0}\sin\Theta$.

The **boundary conditions** for the solution of the zeroth- and first-order pressure fields follow. Note that in those boundaries where the pressure is fixed, say at ambient condition, the perturbed pressures must vanish, i.e. a homogeneous boundary condition. Hence,

$$P_0(\Theta_l\,,0<z<L)=P_S\,;\;P_0\,(\Theta_t\,,\,0<z<L)=P_a$$
$$\Theta_l\le\Theta\le\Theta_t:P_0\left(\Theta,0\right)=P_a\;;\quad P_0\left(\Theta,L\right)=P_a\,; \tag{13a}$$

$$\left[P_X=P_Y=P_{\dot X}=P_{\dot Y}=P_{\ddot X}=P_{\ddot Y}\right]_{(\Theta_l,z),(\Theta_t,z),(\Theta,0),(\Theta,L),}=0 \tag{13b}$$

---

[5] The physical units of each perturbed pressure differ. For example,
$(P_X,P_Y)\leftarrow\left[Pa/m\right],(P_{\dot X},P_{\dot Y})\leftarrow\left[Pa/{m/s}\right],\,(P_{\ddot X},P_{\ddot Y})\leftarrow\left[Pa/{m/s^2}\right]$

At the inception of the film rupture or cavitation zone (Θ_c), P_0=P_{cav}, and $\left(\partial P_0 / \partial \Theta\right) = 0$. At this location, the first-order pressure fields also vanish, i.e. $P_X = P_Y = P_{\dot{X}} = P_{\dot{Y}} = P_{\ddot{X}} = P_{\ddot{Y}} = 0$. Other physical conditions may also apply[6].

The current analysis does not consider a perturbation in the temperature field or the lubricant material properties (density and viscosity). Recall the journal motions are small in amplitude affecting little the steady-state temperature field. However, in bearings and seals operating in the turbulent flow regime, the journal motion does affect the flow condition and hence, there is the need to account for temporal variations in the fluid material viscosity and density, see Notes 10 [6]

Bearing reaction forces and force coefficients

The hydrodynamic pressure field generated in each pad acts on the journal to generate a fluid film reaction force with components $\left(F_X, F_Y\right)$. Integration of the pressure fields gives

$$\begin{bmatrix} F_X \\ F_Y \end{bmatrix} = \sum_{k=1}^{N_{pads}} \begin{bmatrix} F_{X_k} \\ F_{Y_k} \end{bmatrix} = \sum_{k=1}^{N_{pad}} \left\{ \int_0^L \int_{\Theta_l}^{\Theta_t} P_{(\Theta,z,t)_k} \begin{bmatrix} \cos\Theta \\ \sin\Theta \end{bmatrix}_k R\, d\Theta_k\, dz \right\} \tag{14}$$

Substitution of Eq. (10) gives for the k_{th} pad

$$\begin{bmatrix} F_X \\ F_Y \end{bmatrix}_k = \int_0^L \int_{\Theta_1}^{\Theta_t} \left\{ P_0 + P_X \Delta X + P_Y \Delta Y + P_{\dot{X}} \Delta \dot{X} + P_{\dot{Y}} \Delta \dot{Y} + P_{\ddot{X}} \Delta \ddot{X} + P_{\ddot{Y}} \Delta \ddot{Y} \right\}_k \begin{bmatrix} \cos\Theta \\ \sin\Theta \end{bmatrix} R\, d\Theta\, dz \tag{15}$$

The components of a pad reaction force are expressed in terms of stiffness, damping and inertia force coefficients $(K, C, M)_{\alpha\beta=X,Y}$

$$\begin{bmatrix} F_{X(t)} \\ F_{Y(t)} \end{bmatrix}_k = \begin{bmatrix} F_{X_0} \\ F_{Y_0} \end{bmatrix}_k - \begin{bmatrix} K_{XX} & K_{XY} \\ K_{YX} & K_{YY} \end{bmatrix}_k \begin{pmatrix} \Delta X \\ \Delta Y \end{pmatrix} - \begin{bmatrix} C_{XX} & C_{XY} \\ C_{YX} & C_{YY} \end{bmatrix}_k \begin{pmatrix} \Delta \dot{X} \\ \Delta \dot{Y} \end{pmatrix} - \begin{bmatrix} M_{XX} & M_{XY} \\ M_{YX} & M_{YY} \end{bmatrix}_k \begin{pmatrix} \Delta \ddot{X} \\ \Delta \ddot{Y} \end{pmatrix} \tag{16}$$

The bearing pad force coefficients follow from

[6] See for example, Zhang, Y., 1990, "Starting Pressure Boundary Conditions for Perturbed Reynolds Equation," *ASME Journal of Lubrication Technology*, Vol. 112, pp. 551-556.

$$
\begin{bmatrix} K_{XX} & K_{XY} \\ K_{YX} & K_{YY} \end{bmatrix}_k = -\int_0^L \int_{\Theta_1}^{\Theta_t} \begin{bmatrix} \cos\Theta \\ \sin\Theta \end{bmatrix} \begin{bmatrix} P_X & P_Y \end{bmatrix}_k R\, d\Theta\, dz;
$$

$$
\begin{bmatrix} C_{XX} & C_{XY} \\ C_{YX} & C_{YY} \end{bmatrix}_k = -\int_0^L \int_{\Theta_1}^{\Theta_t} \begin{bmatrix} \cos\Theta \\ \sin\Theta \end{bmatrix} \begin{bmatrix} P_{\dot{X}} & P_{\dot{Y}} \end{bmatrix}_k R\, d\Theta\, dz; \tag{17}
$$

$$
\begin{bmatrix} M_{XX} & M_{XY} \\ M_{YX} & M_{YY} \end{bmatrix}_k = -\int_0^L \int_{\Theta_1}^{\Theta_t} \begin{bmatrix} \cos\Theta \\ \sin\Theta \end{bmatrix} \begin{bmatrix} P_{\ddot{X}} & P_{\ddot{Y}} \end{bmatrix}_k R\, d\Theta\, dz;
$$

The individual pad forces and force coefficients add to render the components of reaction force and the force coefficients for the whole bearing, i.e.,

$$
F_\alpha = \sum_{k=1}^{N_{pads}} \left(F_\alpha\right)_k; \;\; K_{\alpha\beta} = \sum_{k=1}^{N_{pads}} \left(K_{\alpha\beta}\right)_k; \;\; C_{\alpha\beta} = \sum_{k=1}^{N_{pads}} \left(C_{\alpha\beta}\right)_k; \;\; M_{\alpha\beta} = \sum_{k=1}^{N_{pads}} \left(M_{\alpha\beta}\right)_k \quad \alpha,\beta = X,Y \tag{18}
$$

Calculation of the bearing static equilibrium position

A fluid film bearing supports an applied load ***W***. This load has components $\left(W_X, W_Y\right)$ along the (X,Y) fixed axes. At the rated operating condition ***W*** produces a static displacement of the journal center, better known as the equilibrium journal eccentricity ***e***, with components $\left(e_{X_0}, e_{Y_0}\right)$. The static balance of forces is

$$
W_X + F_X = 0, \;\; W_Y + F_Y = 0 \tag{19}
$$

Most fluid film bearing analyses predict the bearing reaction forces due to specified journal center static displacements. Thus, in practice, an iterative procedure is implemented to predict the journal equilibrium position given the applied load.

Let the journal operate with eccentricity $\left(e_X, e_Y\right)_j$ at the j_{th} iteration and giving the bearing reaction force components $\left(F_X, F_Y\right)_j$. Then, corrections $\left(\delta e_X, \delta e_Y\right)_j$ to the journal eccentricity that will render reaction forces converging towards the applied external load are given by the Newton-Raphson procedure

$$\begin{bmatrix} \delta e_{X_j} \\ \delta e_{Y\,j} \end{bmatrix} = \begin{bmatrix} K_{XX} & K_{XY} \\ K_{YX} & K_{YY} \end{bmatrix}_j^{-1} \begin{bmatrix} W_X + F_{X_j} \\ W_Y + F_{Y_j} \end{bmatrix} \tag{20a}$$

and

$$\begin{bmatrix} e_{X_{j+1}} \\ e_{Y\,j+1} \end{bmatrix} = \begin{bmatrix} e_{X_j} \\ e_{Y\,j} \end{bmatrix} + \begin{bmatrix} \delta e_{X_j} \\ \delta e_{Y\,j} \end{bmatrix} \tag{20b}$$

Aboce, the bearing *pseudo or temporal* stiffness coefficients *($K_{\alpha\beta=X,Y}$)* are evaluated at $\left(e_X, e_Y\right)_j$.

Upon convergence, the differences in forces in Eq. (19) become negligible, i.e. *$(W+F)_{X,Y} \to 0$;* and the stiffness coefficients are those of the bearing at its equilibrium position.

Note that the bearing reaction forces are highly nonlinear functions of the journal position or eccentricity function; thus, convergence of the Newton-Raphson algorithm relies heavily on the closeness of the initial journal eccentricity components to the actual equilibrium eccentricity. Of course, the fact noted is common in the solution of any nonlienar system of equations.

Generalization of the perturbation method

Consider small amplitude harmonic journal motions $\left(\Delta e_X, \Delta e_Y\right)$ with whirl frequency ω about the equilibrium position $\left(e_{X_0}, e_{Y_0}\right)$. The film thickness *(h)* is the real part of the following expression

$$h = h_0 + \left[\Delta e_X \cos\Theta + \Delta e_Y \sin\Theta\right] e^{\mathbf{i}\omega t} = h_0 + \Delta e_\sigma h_\sigma e^{\mathbf{i}\omega t} \;;\; _{\sigma=X,Y};\;\; \mathbf{i} = \sqrt{-1} \tag{21}$$

with h_0 as the equilibrium film thickness at $\left(e_{X_0}, e_{Y_0}\right)$, and $h_X = \cos\Theta,\; h_Y = \sin\Theta$. Note that,

$$\frac{\partial h}{\partial t} = \frac{\partial\left(h_0 + \Delta e_\sigma h_\sigma e^{\mathbf{i}\omega t}\right)}{\partial t} = \mathbf{i}\,\omega \Delta e_\sigma h_\sigma\, e^{\mathbf{i}\omega t},\;\; \frac{\partial^2 h}{\partial t^2} = -\omega^2 \Delta e_\sigma h_\sigma\, e^{\mathbf{i}\omega t} \tag{22}$$

The pressure field is written as the superposition of zeroth and first order fields,

$$P = P_0 + \Delta e_\sigma P_\sigma e^{\mathbf{i}\omega t} \;;\; _{\sigma=X,Y}. \tag{23}$$

The zeroth-order (P_0) is the equilibrium pressure field satisfying

$$L(P_0) = \frac{1}{R^2}\frac{\partial}{\partial\Theta}\left(\frac{h_0^3}{12\,\mu}\frac{\partial P_0}{\partial\Theta}\right) + \frac{\partial}{\partial z}\left(\frac{h_0^3}{12\,\mu}\frac{\partial P_0}{\partial z}\right) = \frac{\Omega R}{2}\frac{\partial h_0}{R\,\partial\Theta} \tag{24=12a}$$

and the first-order complex pressure fields $P_{\sigma=X,Y}$ due to the journal center motions satisfy

$$L(P_\sigma) = \frac{\Omega}{2}\frac{\partial h_\sigma}{\partial \Theta} + \left\{\boldsymbol{i} - \left(\frac{\rho h_0^2 \omega}{12\mu}\right)\right\}\omega h_\sigma - \frac{\partial}{R\partial\Theta}\left(\frac{3h_0^2 h_\sigma}{12\mu}\frac{\partial P_0}{R\partial\Theta}\right) - \frac{\partial}{\partial z}\left(\frac{3h_0^2 h_\sigma}{12\mu}\frac{\partial P_0}{\partial z}\right); \; {\scriptstyle \sigma=X,Y}$$

or (25)

$$L(P_\sigma) = \left\{\boldsymbol{i} - \left(\frac{\rho h_0^2 \omega}{12\mu_{(T)}}\right)\right\}\omega h_\sigma + \frac{\partial}{R\partial\Theta}\left(\frac{\Omega R}{2}h_\sigma - \frac{3h_0^2}{12\mu_{(T)}}h_\sigma\frac{\partial P_0}{R\partial\Theta}\right) - \frac{\partial}{\partial z}\left(\frac{3h_0^2 h_\sigma}{12\mu_{(T)}}\frac{\partial P_0}{\partial z}\right)$$

Above $\left(\frac{\rho h_0^2 \omega}{12\mu}\right) = \mathrm{Re}_s$ represents a local squeeze film Reynolds number.

The F_X and F_Y components of the fluid film bearing reaction force are

$$F_\sigma = \int_0^L\int_\Theta P\, h_\sigma\; R\, d\Theta\; dz = \int_0^L\int_\Theta \left\{P_0 + \Delta e_\sigma P_\sigma e^{\boldsymbol{i}\omega t}\right\} h_\sigma\; R\, d\Theta\; dz = F_{\sigma_0} - Z_{\sigma\beta}\,\Delta e_\sigma\, e^{\boldsymbol{i}\omega t}\;;\; {\scriptstyle \sigma,\beta=X,Y} \quad (26)$$

where the components of the static (equilibrium) bearing reaction force at journal position $\left(e_{X_0}, e_{Y_0}\right)$ are

$$F_{\sigma_0} = \int_0^L\int_\Theta P_0\, h_\sigma\; R\; d\Theta\; dz = \text{-}W_\sigma \;;\; {\scriptstyle \sigma=X,Y} \quad (27)$$

and the bearing impedances ($Z_{\beta\sigma}$) rendering the stiffness, damping and inertia force coefficients, $(K, C, M)_{\alpha\beta=X,Y}$, are evaluated from the real and imaginary parts of

$$Z_{\beta\sigma} = \left(K_{\beta\sigma} - \omega^2 M_{\beta\sigma}\right) + \boldsymbol{i}\,\omega\, C_{\beta\sigma} = -\int_0^L\int_\Theta P_\sigma\, h_\beta\, R\, d\Theta\; dz\;;\quad {\scriptstyle \beta,\sigma=X,Y} \quad (28)$$

Numerical solution of film pressure equations: equilibrium and first-order

The finite element method (FEM) is well suited for the numerical solution of elliptic type differential equations such as Reynolds Equation. Complicated geometrical domains are well represented by finite elements, hence its major advantage over other methods such as finite differences. Another advantage becomes apparent later as the systems of equations for solution of the zeroth and first order pressure fields have the same (global) fluidity matrix. This feature allows the most rapid evaluation of the bearing dynamic force coefficients.

Figure 6 depicts a flow region divided into a collection of N_{em} four-noded isoparametric finite elements. The pressure over an element (Ω^e) is given by a linear combination of nodal values $\left\{\overline{P}_i\right\}_{=1}^{n_{pe}}$ and bilinear shape functions $\left\{\Psi_i^e\right\}_{=1}^{n_{pe}}$, i.e.

$$P_0^e = \sum_{i=1}^{n_{pe}} \Psi_i^e \overline{P}_{0_i}^e \;, \quad P_\sigma^e = \sum_{i=1}^{n_{pe}} \Psi_i^e \overline{P}_{\sigma_i}^e \;; \quad \sigma = X, Y \tag{29}$$

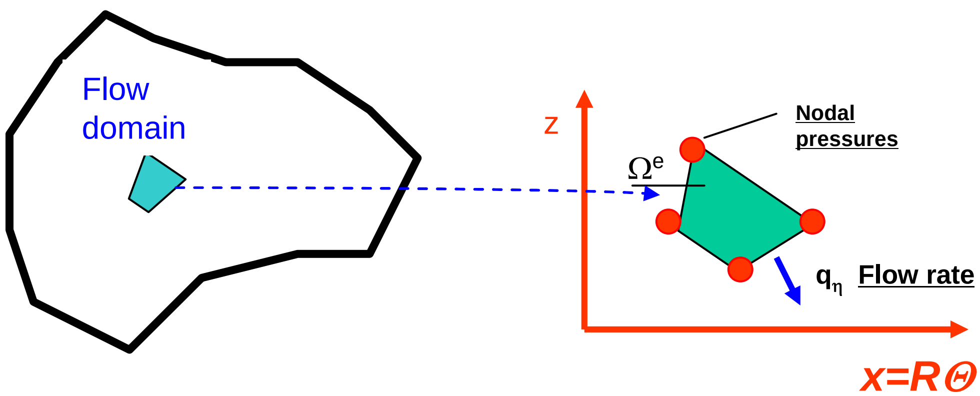

Figure 6. Depiction of general domain of flow field and finite element representation

The Galerkin formulation [15] reduces the PDE (12a) for the equilibrium pressure field P_0 within a finite element (Ω^e) into the algebraic system of linear equations

$$\left[\mathbf{k}\right]^{\mathbf{e}}\left\{\overline{\mathbf{P}}_{\mathbf{0}}\right\}_{\mathbf{G}} = -\left\{\mathbf{q}_0\right\}^{\mathbf{e}} + \left\{\mathbf{f}_0\right\}^{\mathbf{e}}: \qquad \sum_{j=1}^{n_{pe}} k_{ij}^e \, \overline{P}_{0_j}^e = -\left(q_0\right)_i^e + \left(f_0\right)_i^e \;; \; i,j=1,N_{pe} \tag{30}$$

where the coefficients of the element fluidity matrix $\left[\mathbf{k}\right]^e$ are

$$k_{ij}^e = k_{ji}^e = \iint_{\Omega^e} \left[\left(\frac{h_0^3}{12\mu_{(T)}} \right)^e \left\{ \frac{\partial \Psi_i}{\partial x} \frac{\partial \Psi_j}{\partial x} + \frac{\partial \Psi_i}{\partial z} \frac{\partial \Psi_j}{\partial z} \right\}^e \right] dx\, dz \qquad i,j=1,..N_{pe} \tag{31}$$

and the right hand side vectors denote the shear flow effect and nodal flow rates,

$$f_{0_i}^e = \frac{\Omega R}{2} \iint_{\Omega^e} \left(h_0 \frac{\partial \Psi_i}{\partial x} \right)^e dx\, dz \;; \qquad q_{0_i}^e = \oint_{\Gamma^e} \Psi_i^e q_{\eta_0} d\Gamma^e \qquad i=1,..N_{pe} \tag{32}$$

with

$$q_{\eta_0} = -\frac{h_0^3}{12\mu_{(T)}} \frac{\partial P_0}{\partial \eta} + \frac{h_0 \Omega R}{2} \eta_x \tag{33}$$

as the flow through the element boundary (Γ^e). Note above that the fluid viscosity is a function of the temperature, $\mu = \mu_S \, e^{-\alpha_v (T - T_S)}$; thys, varying over the flow domain.

The integrals in Eqns. (31, 32) are evaluated numerically over a master isoparametric element ($\hat{\Omega}$) with normalized coordinates. Reddy and Gartling [16] explain the coordinate transformation and numerical integration procedure using Gauss-Legendre quadrature formulas.

Eqns. (30) are assembled over the whole flow domain and then condensed by enforcing the corresponding boundary conditions. The resultant global set of equations is

$$[\mathbf{k}]_{\mathbf{G}} \left\{\bar{\mathbf{P}}_{\mathbf{0}}\right\}_{\mathbf{G}} = -\{\mathbf{Q}\}_{\mathbf{G}} + \{\mathbf{F}\}_{\mathbf{G}} \tag{34}$$

where $[\mathbf{k}]_{\mathbf{G}} = \bigcup_{e=1}^{Nem} [\mathbf{k}]^e$, $\{\mathbf{Q}\}_{\mathbf{G}} = \bigcup_{e=1}^{Nem} \{\mathbf{q}\}^{\mathbf{e}}$, $\{\mathbf{F}\}_{\mathbf{G}} = \bigcup_{e=1}^{Nem} \{\mathbf{f}\}^{\mathbf{e}}$. The global fluidity matrix $[\mathbf{k}]_{\mathbf{G}}$ is symmetric, easily decomposed into its upper and lower triangular form (Cholesky algorithm), i.e.

$$[\mathbf{k}]_{\mathbf{G}} = [\mathbf{L}]_{\mathbf{G}} [\mathbf{U}]_{\mathbf{G}} = [\mathbf{L}]_{\mathbf{G}} [\mathbf{L}]_{\mathbf{G}}^{\mathbf{T}} \tag{35}$$

A process of back- and forward-substitutions then renders the discrete zeroth order pressure field $\left\{\bar{\mathbf{P}}_{\mathbf{0}}\right\}_{\mathbf{G}}$:

$$[\mathbf{L}]_{\mathbf{G}} \left([\mathbf{L}]_{\mathbf{G}}^{\mathbf{T}} \left\{\bar{\mathbf{P}}_{\mathbf{0}}\right\}_{\mathbf{G}} \right) = -\{\mathbf{Q}\}_{\mathbf{G}} + \{\mathbf{F}\}_{\mathbf{G}} \tag{36}$$

Note that $\{\mathbf{Q}\}_{\mathbf{G}} = \mathbf{0}$ denotes the addition of flow rates at a node. Hence the components of this vector are nil at each internal node of the finite element domain.

A similar procedure follows for solution of the perturbed (dynamic) pressure fields, P_X and P_Y, due to journal harmonic displacements $(\Delta e_X, \Delta e_Y)$ with whirl frequency ω. PDEs (25) become

$$\sum_{j=1}^{n_{pe}} k_{ij}^e \bar{P}_{\sigma_j}^e = (f_\sigma)_i^e - \sum_{j=1}^{n_{pe}} (S_\sigma)_{ij}^e \, \bar{P}_{0_j}^e - (q_\sigma)_i^e \quad ; \quad \sigma = X, Y \qquad {}_{i,j=1,..N_{pe}} \tag{37}$$

with $h_X = \cos\Theta$, $h_Y = \sin\Theta$, $\mathbf{i} = \sqrt{-1}$. Defining $\Psi_{i,x} = {\partial \Psi_i}/{\partial x}$ and $\Psi_{i,z} = {\partial \Psi_i}/{\partial z}$. Above, for perturbations along the X-direction,

$$[\mathbf{k}]^{\mathbf{e}} \left\{\bar{\mathbf{P}}_X\right\}_{\mathbf{G}} = \{\mathbf{f}_X\}^{\mathbf{e}} - [\mathbf{S}_X]^{\mathbf{e}} \left\{\bar{\mathbf{P}}_{\mathbf{0}}\right\}_{\mathbf{G}} - \{\mathbf{q}_X\}^{\mathbf{e}} \tag{37a}$$

for example.

In Equations (37)

$$\left(f_\sigma\right)_i^e = \frac{\Omega R}{2}\iint_{\Omega^e}\left(h_\sigma \Psi_{i,x}^e\right)\, dx\, dz + \iint_{\Omega^e} h_\sigma\left[\frac{\rho\,\omega^2 h_0^2}{12\,\mu_{(T)}}\right]^e \Psi_i^e\; dx\, dz\; - \mathbf{i}\,\omega \iint_{\Omega^e} h_\sigma\left[\Psi_i^e\;\right] dx\, dz$$

$$\left(S_\sigma\right)_{ij}^e = \iint_{\Omega^e}\left(\frac{3\,h_0^2\, h_\sigma}{12\,\mu_{(T)}}\right)^e \left\{\Psi_{i,x}\Psi_{j,x} + \Psi_{i,z}\Psi_{j,z}\right\}^e dx\, dz\,, \qquad i,j=1,..N_{pe} \tag{38}$$

$$\left(q_\sigma\right)_i^e = \oint_{\Gamma^e} \Psi_i^e \left(q_\sigma\right)_\eta\, d\,\Gamma^e\;; \qquad \left(q_\sigma\right)_\eta = -\frac{h_0^3}{12\,\mu_{(T)}}\frac{\partial P_\sigma}{\partial \eta} - \frac{3\,h_0^2\, h_\sigma}{12\,\mu_{(T)}}\frac{\partial P_0}{\partial \eta} + \frac{\Omega R}{2} h_\sigma\, \eta_x$$

The assembly process of the first order *FE* equations renders a fluidity matrix identical to that for the equilibrium pressure field. Thus, the perturbed pressure fields can be calculated rapidly since the global fluidity matrix $\left[\mathbf{k}\right]_{\mathbf{G}}$ is originally obtained and decomposed in the procedure to find the equilibrium pressure field $\left\{\overline{\mathbf{P}}_{\mathbf{0}}\right\}_{\mathbf{G}}$, see Eq. (36).

In practice, the process does not require specification of a whirl frequency (ω) nor conducting several calculations to discern the stiffnesses from the mass coefficients.

For $\left(P_X, P_Y\right)$ from Eqs. (12b):

$$\sum_{j=1}^{n_{pe}} k_{ij}^e \overline{P}_{\sigma_j}^e = \left(f_\sigma\right)_i^e - \sum_{j=1}^{n_{pe}} \left(S_\sigma\right)_{ij}^e\, \overline{P}_{0_j}^e - \left(q_\sigma\right)_i^e \quad ; \quad \sigma = X,\, Y \qquad i=1,..N_{pe} \tag{39a}$$

$$\left(f_\sigma\right)_i^e = \frac{\Omega R}{2}\iint_{\Omega^e}\left(h_\sigma \Psi_{i,x}^e\right)\, dx\, dz\,;\; \left(S_\sigma\right)_{ij}^e = \iint_{\Omega^e}\left(\frac{3\,h_0^2\, h_\sigma}{12\,\mu_{(T)}}\right)^e \left\{\Psi_{i,x}\Psi_{j,x} + \Psi_{i,z}\Psi_{j,z}\right\}^e dx\, dz \tag{39b}$$

To make the global system of equations

$$\left[\mathbf{L}\right]_{\mathbf{G}}\left(\left[\mathbf{L}\right]_{\mathbf{G}}^{\mathbf{T}}\left\{\overline{\mathbf{P}}_{\boldsymbol{\sigma}}\right\}_{\mathbf{G}}\right) = -\left\{\mathbf{Q}\right\}_{\mathbf{G}} + \left\{\mathbf{F}_{\boldsymbol{\sigma}}\right\}_{\mathbf{G}} - \left[\mathbf{S}_{\boldsymbol{\sigma}}\right]_{\mathbf{G}}\left\{\mathbf{P}_{\mathbf{0}}\right\}_{\mathbf{G}} \tag{39c}$$

For $\left(P_{\dot{X}}, P_{\dot{Y}}\right)$ from Eqs. (12c):

$$\sum_{j=1}^{n_{pe}} k_{ij}^e \overline{P}_{\dot{\sigma}_j}^e = \left(f_{\dot{\sigma}}\right)_i^e - \left(q_{\dot{\sigma}}\right)_i^e \quad ; \quad \dot{\sigma} = \dot{X},\, \dot{Y} \qquad i=1,..N_{pe} \tag{40a}$$

$$\left(f_{\dot{\sigma}}\right)_i^e = -\iint_{\Omega^e} h_\sigma\left[\Psi_i^e\;\right] dx\, dz \qquad i=1,..N_{pe} \tag{40b}$$

Giving the global system of equations

$$[\mathbf{L}]_{\mathbf{G}}\left([\mathbf{L}]_{\mathbf{G}}^{\mathbf{T}}\{\overline{\mathbf{P}}_{\dot{\boldsymbol{\sigma}}}\}_{\mathbf{G}}\right)=-\{\mathbf{Q}\}_{\mathbf{G}}+\{\mathbf{F}_{\dot{\boldsymbol{\sigma}}}\}_{\mathbf{G}} \tag{40c}$$

For $\left(P_{\ddot{X}}, P_{\ddot{Y}}\right)$ from Eqs. (12c):

$$\sum_{j=1}^{n_{pe}} k_{ij}^{e}\overline{P}_{\ddot{\sigma}_j}^{e} = \left(f_{\ddot{\sigma}}\right)_i^e - \left(q_{\ddot{\sigma}}\right)_i^e \quad ; \quad {\scriptstyle \ddot{\sigma}=\ddot{X},\,\ddot{Y}} \qquad {\scriptstyle i=1,..N_{pe}} \tag{41a}$$

$$\left(f_{\ddot{\sigma}}\right)_i^e = -\iint_{\Omega^e} h_\sigma \left[\frac{\rho\, h_0^2}{12\,\mu_{(T)}}\right]^e \Psi_i^e \; dx\, dz \qquad {\scriptstyle i=1,..N_{pe}} \tag{41b}$$

Giving the system of equations

$$[\mathbf{L}]_{\mathbf{G}}\left([\mathbf{L}]_{\mathbf{G}}^{\mathbf{T}}\{\overline{\mathbf{P}}_{\ddot{\boldsymbol{\sigma}}}\}_{\mathbf{G}}\right)=-\{\mathbf{Q}\}_{\mathbf{G}}+\{\mathbf{F}_{\ddot{\boldsymbol{\sigma}}}\}_{\mathbf{G}} \tag{41c}$$

Solution of the system of equations for the first order fields is performed quickly with the procedure

$$\begin{aligned}
&[\mathbf{L}]_{\mathbf{G}}\left([\mathbf{L}]_{\mathbf{G}}^{\mathbf{T}}\{\mathbf{X}\}_{\mathbf{G}}\right)=\{\mathbf{Y}\}_{\mathbf{G}}\\
&[\mathbf{L}]_{\mathbf{G}}\{\mathbf{Z}\}_{\mathbf{G}}=\{\mathbf{Y}\}_{\mathbf{G}} \rightarrow \text{find}\,\{\mathbf{Z}\}_{\mathbf{G}}\\
&[\mathbf{L}]_{\mathbf{G}}^{\mathbf{T}}\{\mathbf{X}\}_{\mathbf{G}}=\{\mathbf{Z}\}_{\mathbf{G}} \rightarrow \text{find}\,\{\mathbf{X}\}_{\mathbf{G}}
\end{aligned} \tag{42}$$

which does not require inversion of matrices but only 2-N forward and backward substitutions.

Numerical solution of the traport equation for fluid film mean temperature

The transport of energy equation (3) is of parabolic type. Hence, a control volume method with upwinding [17] is chosen to solve for the temperature field. Figure 7 depicts the control volume for integration of the thermal energy transport Eq. (3). Note that, in accordance with practice and measurements, the fluid bulk-temperature (T) does not vary along the bearing axial length. In the figure, $\{T^e, T^w$ and $T^n\}$ are temperatures at the east, west and north faces of the P-control volume; while $\{T_E, T_W, T_P\}$ are nodal temperatures at the center of the control-volumes.

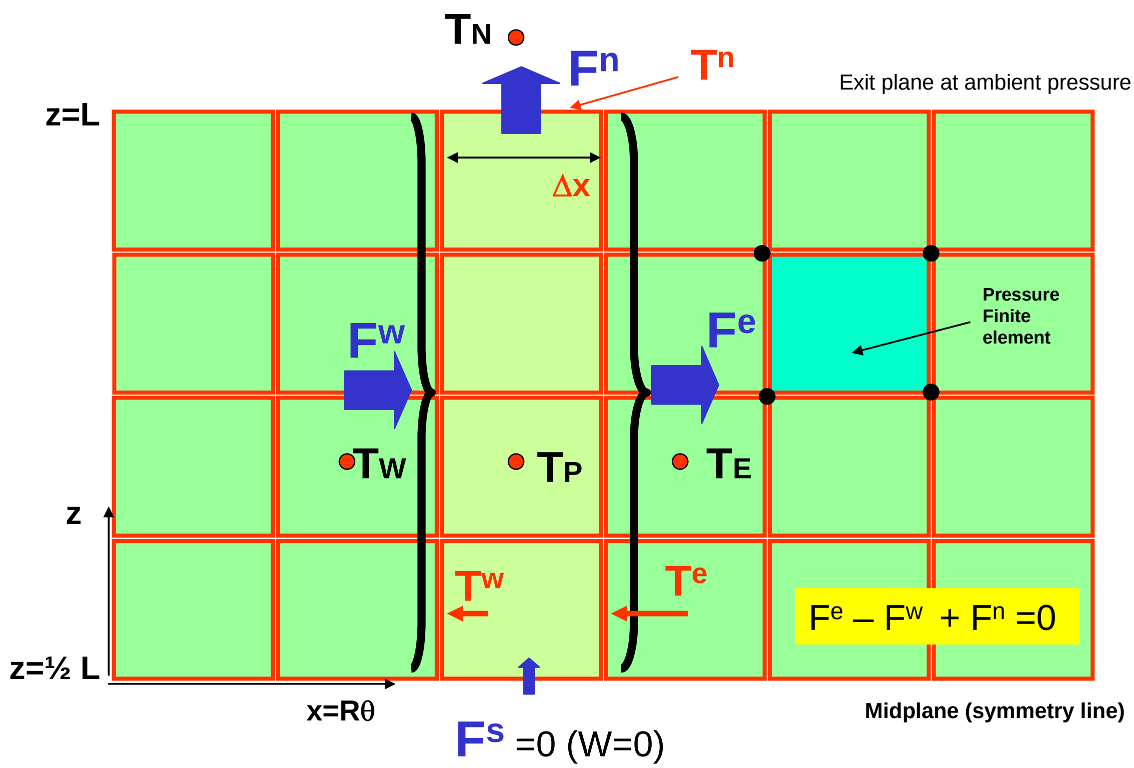

Figure 7. Control volumes for integration of energy transport equation (*F*: flow, *T*: temperature)

Integration of the energy transport Eq. **(**3**)** over ½ axial length of the bearing (*T*-control volume) leads to:

$$C_v\left[\int_{L/2}^{L}\left(\rho h U T\right)_w^e dz+\int_w^e\left(\rho h W T\right)_{z=L/2}^{L} dx\right]=\int_{L/2}^{L}\left(S-Q_s\right)dz\,dx \tag{43}$$

with the source (energy dissipation) term $S=\frac{12\,\mu_{(T)}}{h}\left(W^2+\frac{\Omega^2R^2}{12}+\left[U-\frac{\Omega R}{2}\right]^2\right)$ (44)

and heat flow into the bearing and journal surfaces $Q_s=\bar{h}_B\left(T-T_B\right)+\bar{h}_J\left(T-T_J\right)$ (45)

Since the film temperature is regarded as constant along the axial direction, Eq. (43) reduces to

$$C_v\left[T^e\int_{L/2}^{L}\left(\rho h U\right)^e dz-T^w\int_{L/2}^{L}\left(\rho h U\right)^w dx+T^n\int_w^e\left(\rho h W\right)_{z=L} dx\right]=\int_{L/2}^{L}\left(S-Q_s\right)dz\,dx \tag{46}$$

Recall that the axial flow velocity is null[7] at the midplane of a bearing pad, i.e., W=0 at z=0. Define mass flow rates (F) through the control volume faces as

$$F^e = \int_{L/2}^{L} (\rho h U)^e \, dz \simeq \sum_{J}^{Ne_z} (\rho h U)_J^e \, \Delta z,$$
$$F^w = \int_{L/2}^{L} (\rho h U)^w \, dz \simeq \sum_{J}^{Ne_z} (\rho h U)_J^w \, \Delta z, \tag{47}$$
$$F^n = \int_w^e (\rho h W)_{z=L/2} \, dx; \;\; F^s = \int_w^e (\rho h W)_{z=0} \, dx = 0$$

where Ne_z is the number of P-finite elements along the axial direction. The source term from shear drag power is

$$S^P = \int_{L/2}^{L} S \, dz \, dx \simeq \sum_{J}^{Ne_z} \left(\frac{12\,\mu_{(T)}}{h} \left(W^2 + \frac{\Omega^2 R^2}{12} + \left[U - \frac{\Omega R}{2} \right]^2 \right) \right)_J^P \Delta z \, \Delta x \,, \tag{48a}$$

From mass flow continuity $\left[F^e - F^w + F^n - 0 \right]$ =0. Assume for simplicity that the bearing (T_B) and journal (T_J) temperatures are constant along the axial direction. An identical statement is made for the heat convection coefficients $\left(\bar{h}_B, \bar{h}_J \right)$. Then,

$$Q^P = \int_{L/2}^{L} Q_s \, dz \, dx \simeq T_P \left(\bar{h}_B + \bar{h}_J \right) \frac{L}{2} \Delta x - \left(\bar{h}_B T_B + \bar{h}_J T_J \right) \frac{L}{2} \Delta x \tag{48b}$$

With the definitions above, the discretized algebraic form of the energy transport equation is:

$$\boxed{C_v \left[F^e T^e - F^w T^w + F^n T^n \right] = S^P - Q^P} \tag{49}$$

Implementation of the **upwind scheme** [17] for the thermal flux transport terms gives:

$$F^e T^e = \left[\!\left[F^e, 0 \right]\!\right] T_P - \left[\!\left[-F^e, 0 \right]\!\right] T_E$$
$$F^w T^w = \left[\!\left[F^w, 0 \right]\!\right] T_W - \left[\!\left[-F^w, 0 \right]\!\right] T_P \tag{50}$$
$$F^n T^n = \left[\!\left[F^n, 0 \right]\!\right] T_P - \left[\!\left[-F_n, 0 \right]\!\right] T_N$$

with $\left[\!\left[a, 0 \right]\!\right] = \frac{1}{2}\left[a + |a| \right]$; $\left[\!\left[-a, 0 \right]\!\right] = \frac{1}{2}\left[-a + |a| \right]$; $\left[\!\left[a, 0 \right]\!\right] - \left[\!\left[-a, 0 \right]\!\right] = a$;

7 This is because the pressure field is symmetric along the axial direction. That is, the peak pressure occurs at the axial mid-plane of the bearing

where T_N is a fluid sump temperature (outside) of the bearing discharge plane[8].

Substitution of Eq. (50) into Eq. (49) renders the control-volume integral form of the energy transport equation

$$a_p\,T_P = a_w\,T_W + a_e\,T_E + a_n\,T_N + S^P + Q_{JB}^P \tag{51}$$

where
$$a_e = C_v\left[\!\left[-F^e, 0\right]\!\right];\quad a_w = C_v\left[\!\left[F^w, 0\right]\!\right];\quad a_n = C_v\left[\!\left[-F^n, 0\right]\!\right] \tag{52a}$$

$$a_p = a_e + a_w + a_n + \left(\bar{h}_B + \bar{h}_J\right)\frac{L}{2}\Delta x \tag{52c}$$

$$Q_{JB}^P = \left(\bar{h}_B\,T_B + \bar{h}_J\,T_J\right)\frac{L}{2}\Delta x \tag{52c}$$

The system of equations (51) is easily solved with a simple recursive algorithm. If the lubricant flow is from left to right (*w* to *e*), then $F^w > 0; F^e > 0 \rightarrow a_e = 0$; and the energy transport equation reduces to

$$a_p\,T_P = a_w\,T_W + a_n\,T_N + S^P + Q_{JB}^P \tag{53}$$

If lubricant flows outward at the exit plane $z = ½\,L$, $F^n > 0 \rightarrow a_n = 0$, and the energy transport equation further reduces to

$$a_p\,T_P = a_w\,T_W + S^P + Q_{JB}^P \tag{54}$$

where $a_p = +a_w + \left(\bar{h}_B + \bar{h}_J\right)\frac{L}{2}\Delta x$. This last equation, revealing the parabolic nature of the thermal energy transport, shows the film temperature increases due to shear power dissipation effects. Note that $Q_{JB}^P = 0$ for adiabatic boundaries, i.e. $\left(\bar{h}_B = \bar{h}_J = 0\right)$, i.e. no heat flow into or from the bearing and journal.

The algebraic equations for solutions of the presure and temperature fields are programmed in FORTRAN with a Graphical User Interface in MS Excel® for input of bearing data and operating conditions and output of predictions that include the bearing torque and flow rate, static journal eccentricity, dynamid force coefficients, and the pressure and temperature fields. For completeness in the description, Figure 8 depicts the relationship between a finite element for evaluation of the film pressure and the control-volume for temperature.

[8] $F^n < 0$ means that flow is entering (instead of leaving) the bearing at the exit plane $z = ½\,L$. This condition is not unusual in the zone of lubricant cavitation. However, in practice the value of sump temperature is not well known a-priori.

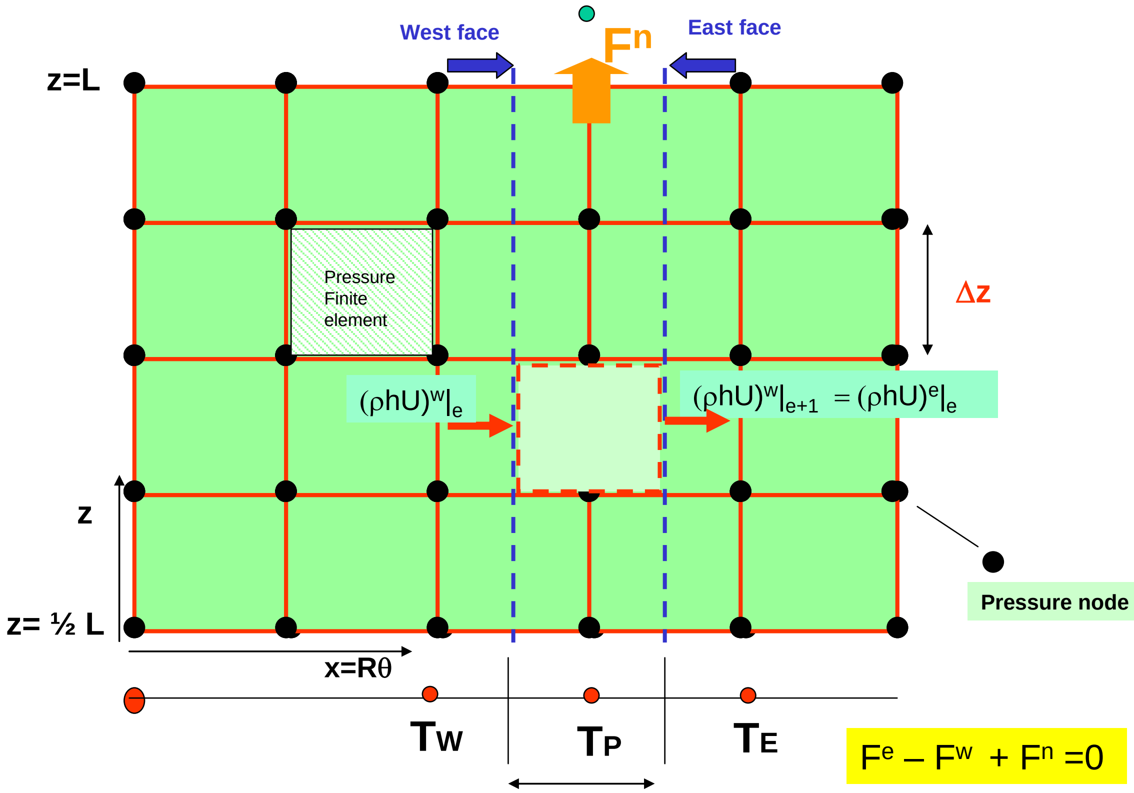

Figure 8. Flow fluxes through faces of temperature-CV and relation to pressure finite elements

Examples

Model predictions for test bearings reported in the literature were obtained. The benchmark cases included one and two grooved journal bearings[9], see refs. [12,13]. In general, the predictions for static load performance conditions, including lubricant temperature rise, load capacity and journal eccentricity are in good agreement with the test data. Note that in the references listed, one or more parameters of importance are ommitted or not published. Hence, the model implemented best practices to obtain accurate results.

Presently, model predictions for the static and dynamic load performance of a pressure dam journal bearing are compared against exhaustive test data acquired in the laboratory, Jughaiman and Childs [18]. Figure 9 shows a schematic view of the bearing configuration and coordinate

[9] A set of slides follows this lecture notes – The slides show details and comparisons of (current) model predictions and test data in Refs. [12,13,18]

system. Table 1 details the geometry of the pressure dam bearing, as detailed in Ref. [18]. Please note that Al-Jughaiman's publication (including his M.s. thesis) misses details on the bearing geometry, lubricant inlet and feed conditions. Note that the pressure dam depth to clearance ratio and dam arc length relative to pad arc length follow standard best practices recommended by Nicholas and Allaire[19].

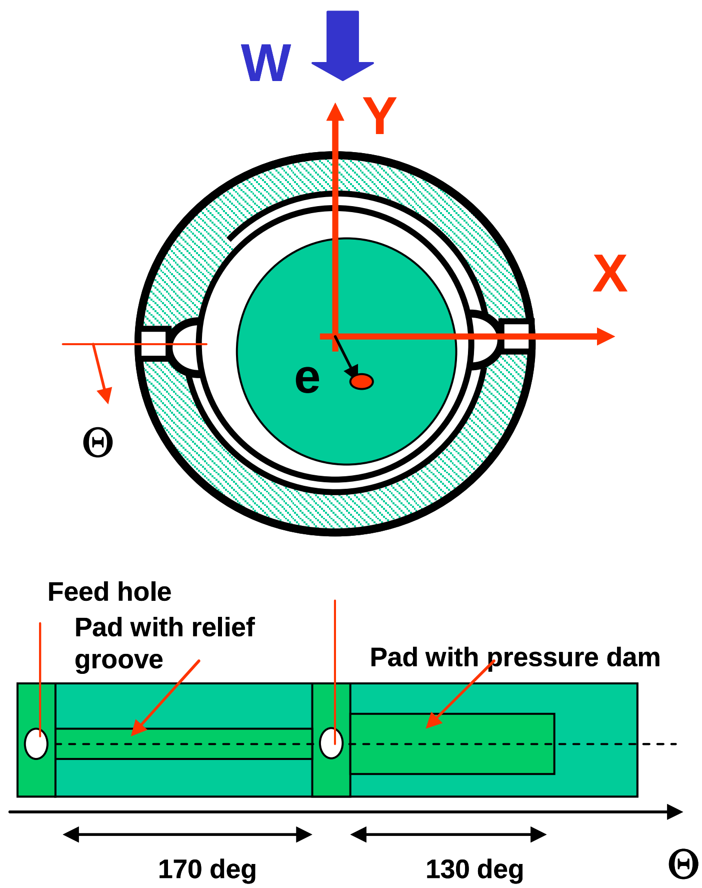

Figure 9. Schematic view of pressure dam bearing with relief groove.

In the experiments, ISO VG 32 lubricant fills the thin film lands of the pressure dam bearing. An air turbine drives the test rigid shaft supported on ball bearings. The test bearing *floats* on the rotating shaft. The tester includes a hydraulic cylinder for static loading, and stinger connections to hydraulic shakers that excite the floating test bearing. The instrumentation includes load cells attached to the shaker stingers, eddy current sensors mounted on the bearing and facing the shaft, and accelerometers attached to the bearing housing. The parameter identification method is based on frequency domain measurements and extracts the force coefficients from curve fits of the real and imaginary parts of the test system impedances.

The maximum load (W) applied equals 12 kN (2,700 lb) which gives a specific pressure (W/LD) = 13.45 bar (~ 200 psi).

Table 1. Dimensions and operating conditions of pressure dam bearing with relief groove tested by Jughaiman and Childs [18]

Journal diameter	D	117.1	mm
Bearing Length	L	76.2	mm
Radial clearance	c	**0.142**	mm
pad arc		**170**	deg
Dam arc length	Θ_D	130	deg
width (0.75 L)	L_D	57.1	mm
depth		**0.4**	**mm**
Reilef groove width	L_R	19.05	mm
depth		**0.1**	**mm**
Lubricant	**ISO VG 32**		
Density	ρ	860	kg/m3
Specific Heat	Cp	2000	J/kg-C
Thermal conductivity	κ	0.13	W/m-C
Viscosity at 45 C	μ	0.028	Pa.s
Visc-temp coefficient	α	0.034	1/C
Inlet oil temperature		**40-55 ?**	C
Inlet oil pressure		**N/A**	bar
Load range		0.1-12	kN
Speed range		4,6,8,10,12	krpm

Closure

Sept 2009: Lecture notes not yet complete. See slide presentation attached.

Nomenclature

c	Nominal film (pad) clearance [m]
c_m	bearing assembled clearance [m]
C_v	Lubricant specific heat [J/kg-K]
$C_{\sigma\beta}$	Bearing damping force coefficients; $_{\sigma,\,\beta = X,\,Y}$ $[\mathrm{N{\cdot}s/m}]$
D	Journal diameter [m]

e_X, e_Y	Journal center eccentric displacements [m]
F_X, F_Y	Fluid film bearing reaction forces [N];
F_S, F_{in}, F_{up},	Mass flow rates: supply, inlet to pad and upstream pad [kg/s]
h	Pad film thickness, $c - r_P \cos(\Theta\text{-}\Theta_P) + e_X \cos(\Theta) + e_Y \sin(\Theta)$ [m]
h_X, h_Y	$\cos(\Theta)$, $\sin(\Theta)$
$\overline{h}_B, \overline{h}_J$	Heat transfer convection coefficients [W/m-K]
$K_{\sigma\beta}$	Bearing stiffness force coefficients; $\sigma, \beta = X, Y$ $[N/m]$
L	Journal bearing axial length [m]
$M_{\sigma\beta}$	Added mass (fluid inertia) coefficients; $\sigma, \beta = X, Y$ $[N/m]$
n_{pe}	Number of nodes per finite element
N_{em}	Number of elements in flow domain
Q_s	heat flow conducted into bearing and journal surfaces [W/m]
P	Film pressure [Pa]
P_a	Ambient pressure [Pa]
P_{cav}	Lubricant cavitation pressure [Pa]
P_S	Supply pressure [Pa]
P_0	Zeroth-order (aquilibrium) pressure [Pa]
P_σ	First-order complex pressure fields; $\sigma, \beta = X, Y$ [Pa/m]
q_η	Volumetric flow rate per unit length [m^2/s]
R	½ D. Journal radius, [m]
Re_s	$\left(\rho\omega h^2 / \mu\right)$. Local squeeze film Reynolds number.
r_p	(c-c_m). Pad preload [m]
S	Mechanical energy dissipation per unit area [W/m^2]
t	Time [s]
T	Lubricant mean flow temperature [degK]
T_S	Supply temperature [degK]
U, W	Lubricant bulk-flow velocities, circumferential and axial [m/s]
W_X, W_Y	Componentsof applied static load, $W = \sqrt{W_X^2 + W_Y^2}$
($x = R\Theta$, y, z)	Coordinate system on plane of bearing (starts at -X)
(X, Y)	Inertial coordinate system
$Z_{\sigma\beta}$	Impedance force coefficients; $\left(K_{\sigma\beta} - \omega^2 M_{\sigma\beta} + \mathbf{i}\omega C_{\sigma\beta}\right)$, $\sigma, \beta = X, Y$ $[N/m]$
α_v	Viscosity-temperature coefficient [1/K]
Δe_X, Δe_Y	Dynamic displacements of journal center [m]
Θ	(x/R). Circumferential coordinate [rad],
Θ_l, Θ_t, Θ_p	Arc pad leading and trailing edges, angle of min. film thickness (offset angle) [rad]
μ	$\mu = \mu_S\, e^{-\alpha_v (T - T_S)}$. Fluid viscosity [Pa-s]
Γ^e	Element boundary
ρ	Fluid density [kg/m^3]
ϕ	Journal attitude angle with respect to static load vector [°]
$\left\{\Psi_i\right\}_{=1}^{n_{pe}}$	Finite element shape functions

Ω	Rotor rotating speed,
ω	whirl frequency $[{}^{rad}/_{s}]$
Ω^e	Finite element sub-domain

Subscripts

S	Supply condition
in	Inlet to pad
n,e,w,s	north, east, west and south of control volume
N,W,E,S	North, east, west and south nodes

Superscripts

e	element

APPENDIX A. MODELS FOR HEAT CONVECTION COEFFICIENTS

Reproduced from Ref.[7]

The Reynolds-Colburn analogy between fluid friction and heat transfer for fully-developed flow determines the heat convection coefficients to accounting for heat flux from the fluid film into the shaft outer surface and from the film into the bearing cartridge. Over the entire laminar/turbulent boundary the *Fanning* friction factor f is:

$$S_t \wp_r^{2/3} = \frac{f}{2} \tag{A.1}$$

where $S_t = \frac{\bar{h}}{\rho C_v U}$ is the *Stanton* number, ρ and C_v are the fluid density and specific heat, and U is a mean flow velocity $\wp_r = \frac{c_p \mu}{\kappa}$ is the *Prandtl* number, and κ and μ are fluid heat conduction coefficient and viscosity, respectively.

From Eq. (A.1), heat convection coefficients $\bar{h}$ for laminar flow are derived from the Nusselt number;

$$Nu = \frac{c\,\bar{h}}{\kappa} = 3\ \wp_r^{1/3} \tag{A.2}$$

while for turbulent flow conditions

$$Nu = \frac{D_{hyd}\bar{h}}{\kappa} = 0.023 Re^{0.8}\ \wp_r^{0.4} \tag{A.3}$$

where $D_{hyd} = \frac{4 \cdot \text{area}}{\text{wetted perimeter}}$ is a hydraulic diameter.

References

[1] Boncompain, R., Fillon M., and Frene, J., 1986, *"Analysis of Thermal Effects in Hydrodynamic Bearings",* ASME Journal of Tribology, 108 (2), pp. 219-224.

[2] Kucinschi, B., ., Fillon M., Pascovici, M., and Frene, J., 2000, "A Transient Thermoelastohydrodynamic Study of Steadily Loaded Plain Journal Bearings using Finite Element Method Analysis", ASME Journal of Tribology, 122, (1), pp. 219-226, 2000.

[3] Reinhart, F., and Lund, J. W., 1975, "The Influence of Fluid Inertia on the Dynamic Properties of Journal Bearings." ASME J. Lubrication Technology, **97**, pp 154-167.

[4] Smith, D. L., 1975, "Journal Bearing Dynamic Characteristics-Effect of Inertia of Lubricant, ***Proc. Inst. Mech. Engrs.,*** Paper No. 21, **179,** Pt.3J, pp 37-44.

[5] San Andrés, L., and Vance, J., 1987, "Effect of Fluid Inertia on Squeeze Film Damper Forces for Small Amplitude Circular Centered Motions," ASLE Transactions, **30**, No. 1, pp. 69-76.

[6] San Andrés, L., 2009, *Modern Hydrodynamic Lubrication Theory*, Notes 10: Thermohydrodynamic Bulk-Flow Model in Thin Film Lubrication, Texas A&M University, http://phn.tamu.edu/me626 [Accessed April 2009]

[7] San Andrés, L., Yang, Z. and Childs, D., 1993, "Thermal Effects in Cryogenic Liquid Annular Seals, I: Theory and Approximate Solutions", ASME Journal of Tribology, **115,** 2, pp. 267-276.

[8] San Andrés, L., and Kerth, J., 2004, "Thermal Effects on the Performance of Floating Ring Bearings for Turbochargers", Journal of Engineering Tribology, Special Issue on Thermal Effects on Fluid Film Lubrication, IMechE Proceedings Part J, **218**, pp. 437-450.

[9] San Andrés, L., 2009, *Modern Hydrodynamic Lubrication Theory*, Notes 6: Cavitation in Liquid Film Bearings, Texas A&M University, http://phn.tamu.edu/me626 [Accessed September 2009]

[10] Pinkus, O., 1990, "Thermal Aspects of Fluid Film Tribology," ASME Press, N.Y.

[11] Lund, J. W., and E.B. Arwas, 1964, "A Simultaneous Solution of the Lubrication and the Energy Equations for Turbulent Journal Bearing Films," MTI Report N^{o} 64-TR-31, MTI, Inc., N.Y.

[12] Ferron, J., Frene, J., and R. Boncompain, 1983, "A Study of the Thermohydrodynamic Performance of a Plain Journal Bearing Comparison between Theory and Experiments", ASME Journal of Tribology, Vol. 105, pp. 422-428,

[13] Brito, F.P., Miranda, A.S., Bouter, J., and Fillon, M., Frene, J., and R. Boncompain, 2007, "Experimental investigation on the influence of Supply temperature and Supply Pressure on the Performance of a Two-Axial Groove Hydrodynamic Journal Bearing", ASME Journal of Tribology, Vol. 129, pp. 98-105.

[14] Lund, J., 1987, "Review of the Concept of Dynamic Coefficients for Fluid Film Journal Bearings," *ASME Journal of Tribology*, Vol. 109, pp. 37- 41.

[15] Klit, P. and Lund, J. W., 1988, "Calculation of the Dynamic Coefficients of a Journal Bearing Using a Variational Approach," *ASME Journal of Tribology*, Vol. 108, pp. 421 - 425.

[16] Reddy J. N., Gartling, D. K., 2001, *The Finite Element Method in Heat transfer and Fluid Dynamics*, CRC Press, Florida, Chap. 2.

[17] Patankar, S.V., 1980, *Numerical Heat Transfer and Fluid Flow,* Hemisphere Pubs, N.Y.

[18] Al-Jughaiman, and Childs, D., 2007, "Static and Dynamic Characteristics for a Pressure-Dam Bearing", ASME Paper GT2007-25577.

[19] Nicholas, J., and Allaire, P., 1980, "Analysis of Step Journal Bearings-Finite Length and Stability," ASLE Transactions, **22**, pp. 197-207.

Additional (numerical analyses) references

The references below detail numerical analyses for hydrodynamic and hydrostatic liquid and gas bearings, rigid pads and tilting pads. Note that tilting pad bearings show frequency dependent force coefficients. The same holds true for gas bearings

Tilting Pad (liquid) bearings

San Andrés, L., "Turbulent Flow, Flexure-Pivot Hybrid Bearings for Cryogenic Applications," ASME Journal of Tribology, Vol. 118, 1, pp. 190-200, 1996

Gas bearings

San Andrés, L., 2006, "Hybrid Flexure Pivot-Tilting Pad Gas Bearings: Analysis and Experimental Validation," ASME Journal of Tribology, **128,** pp. 551-558.

Delgado, A., L., San Andrés, and J. Justak, 2004, "Analysis of Performance and Rotordynamic Force Coefficients of Brush Seals with Reverse Rotation Ability", ASME Paper GT 2004-53614

San Andrés, L., and D. Wilde**,** 2001, "Finite Element Analysis of Gas Bearings for Oil-Free Turbomachinery," Revue Européenne des Eléments Finis, **10** (6/7), pp. 769-790.

Zirkelback, N., and L. San Andrés, 1999, "Effect of Frequency Excitation on the Force Coefficients of Spiral Groove Thrust Bearings and Face Gas Seals," ASME Journal of Tribology, 121(4), pp. 853-863.

Foil Gas bearings

San Andrés, L., and Kim, T.H., "Thermohydrodynamic Analysis of Bump Type gas Foil Bearings: A Model Anchored to Test Data" GT2009-59919

San Andrés, L., and Kim, T.H., 2009, "Analysis of Gas Foil Bearings Integrating FE Top Foil Models," Tribology International, 42(2009), pp. 111-120.

Kim, T.H., and L. San Andrés, 2008, "Heavily Loaded Gas Foil Bearings: a Model Anchored to Test Data," ASME Journal of Engineering for Gas Turbines and Power, Vol. 130(1), pp. 012504-1-8. (ASME Paper GT 2005-68486).

Kim, T.H., and L. San Andrés, 2006, "Limits for High Speed Operation of Gas Foil Bearings," ASME Journal of Tribology, 128, pp. 670-673

San Andrés, L., 1995, "Turbulent Flow Foil Bearings for Cryogenic Applications," ASME Journal of Tribology, 117(1), pp. 185-195.

Hydrostatic/hydrodynamic liquid bearings and seals

San Andrés, L., "Thermohydrodynamic Analysis of Fluid Film Bearings for Cryogenic Applications," AIAA Journal of Propulsion and Power, Vol. 11, 5, pp. 964-972, 1995.

Yang, Z., San Andrés, L. and Childs, D., "Thermal Effects in Cryogenic Liquid Annular Seals, II: Numerical Solution and Results", ASME Journal of Tribology, Vol. 115, 2, pp. 277-284, 1993 (ASME Paper 92-TRIB-5).

San Andrés, L., Yang, Z. and Childs, D., "Thermal Effects in Cryogenic Liquid Annular Seals, I: Theory and Approximate Solutions", ASME Journal of Tribology, Vol. 115, 2, pp. 267-276, 1993 (ASME Paper 92-TRIB-4).

San Andrés, L., "Analysis of Turbulent Hydrostatic Bearings with a Barotropic Fluid," ASME Journal of Tribology, Vol. 114, 4,pp. 755-765,1992.

San Andrés, L., "Fluid Compressibility Effects on the Dynamic Response of Hydrostatic Journal Bearings," WEAR, Vol. 146, pp. 269-283, 1991

San Andrés, L., "Turbulent Hybrid Bearings with Fluid Inertia Effects", ASME Journal of

Tribology, Vol. 112, pp. 699-707,

Computational code

Fortran code : complete – including prediction of inertia force coefficients

GUI (Excel interface) – complete

Examples for calibration:

(pressure and temperature fields)

oil 360 deg journal bearing

Dowson et al. (1966)
Ferron, Frene, Boncompain (1983)
Costa, Fillon (2000 2003)

oil two groove journal bearing

Costa, Fillon (2000 2003)
Brito, Fillon (2006, 2007)

Pressure dam bearing

Childs et al (2007, 2008)
Load capacity & force coefficients

Example 1 : Ferron bearing (1983)

Journal diameter	D	100	mm
Bearing Length	L	80	mm
Radial clearance	c	0.152	mm
Groove width			mm
groove arc length		18	deg
Lubricant			
Density	η	860	kg/m3
Specific Heat	Cp	2000	J/kg-C
Thermal conductivity	η	0.13	W/m-C
Viscosity at 40 C	η	0.0277	Pa.s
Visc-temp coefficient	η	0.034	1/C
Inlet oil temperature		40	C
Inlet oil pressure		0.7	bar
Load range		1kN-10 kN	
Speed range		1-4 kRPM	
Prandtl No		426	
Load No		23.98	
Diffusivity		7.55814E-08	m2/s
Sommerfeld #		$S = \frac{\mu\ N\ L\ D}{W}\left(\frac{R}{C}\right)^2$	

Ferron,J., Frene, J., and R. Boncompain, 1983, "A Study of the Thermohydrodynamic Performance of a Plain Journal Bearing Comparison Between Theory and Experiments", ASME Journal of Tribology, Vol. 105, pp. 422-428,

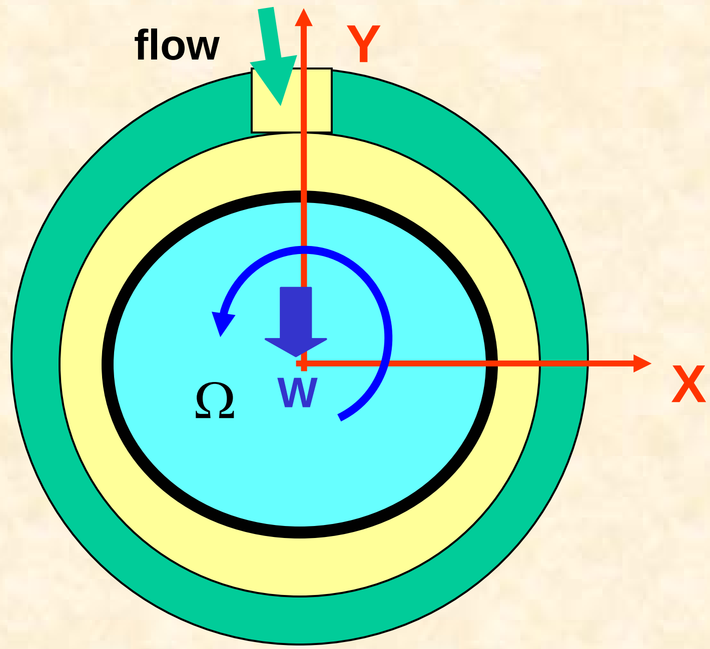

Ferron et al. bearing (1983)

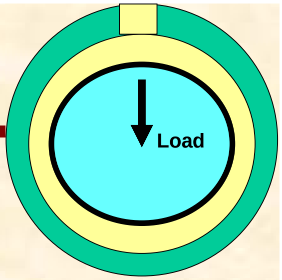

Test data

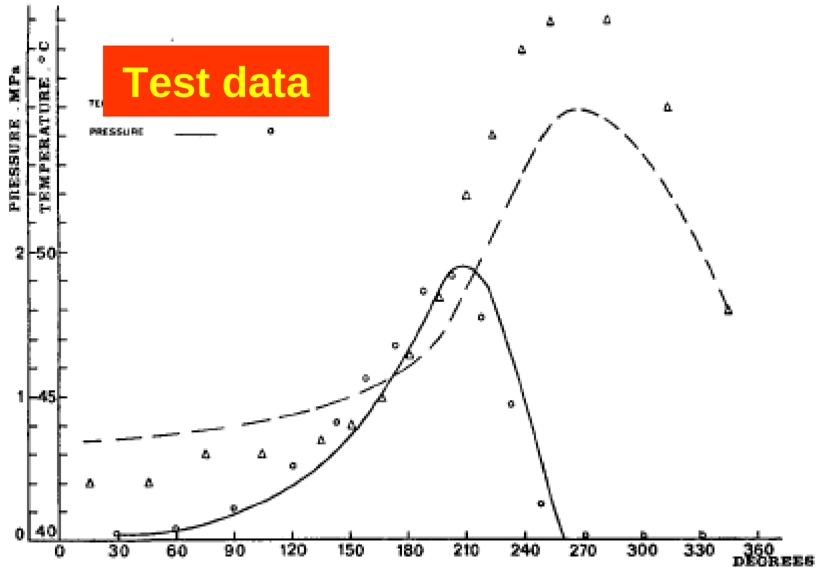

Fig. 6 Pressure and temperature variations in mid-plane at 4000 rmp and under 6000 N

Film temperature

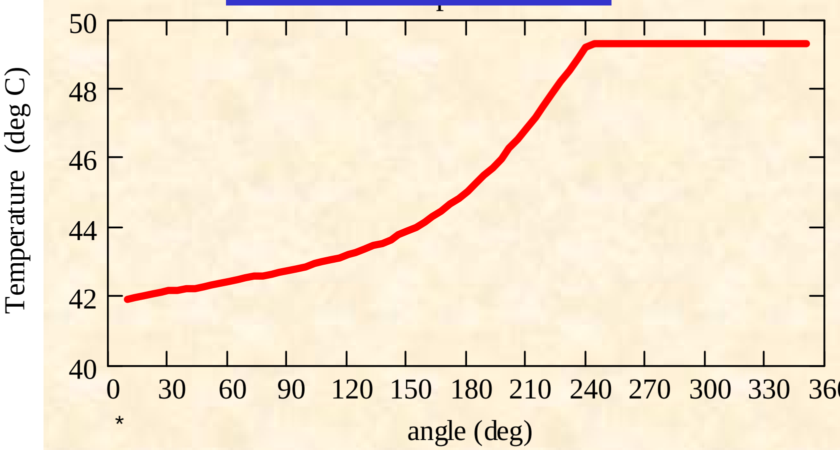

Midplane pressure

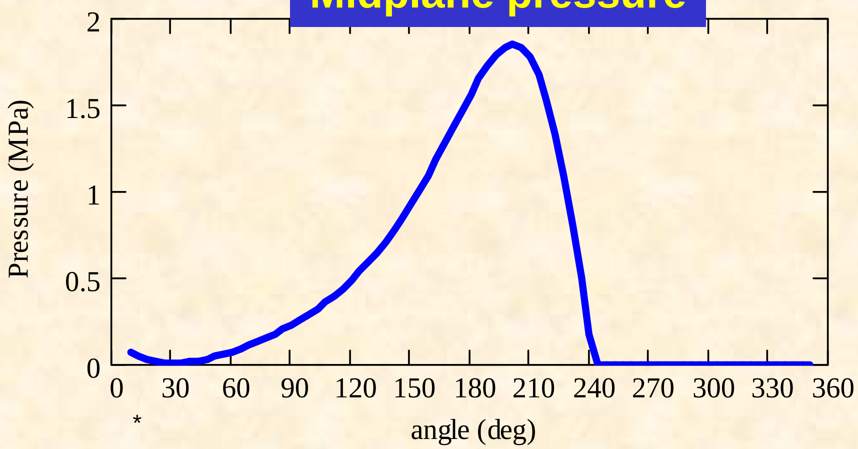

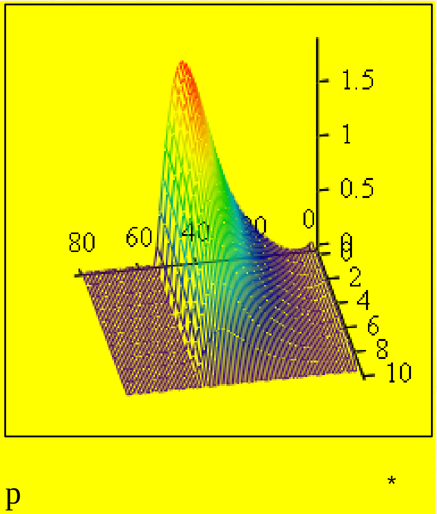

Pressure and temperature fields – 4 kRPM, 6 kN

Ferron et al. bearing (1983)

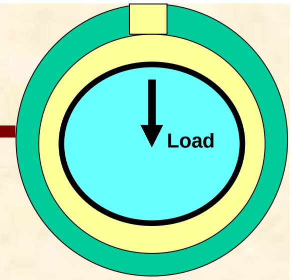

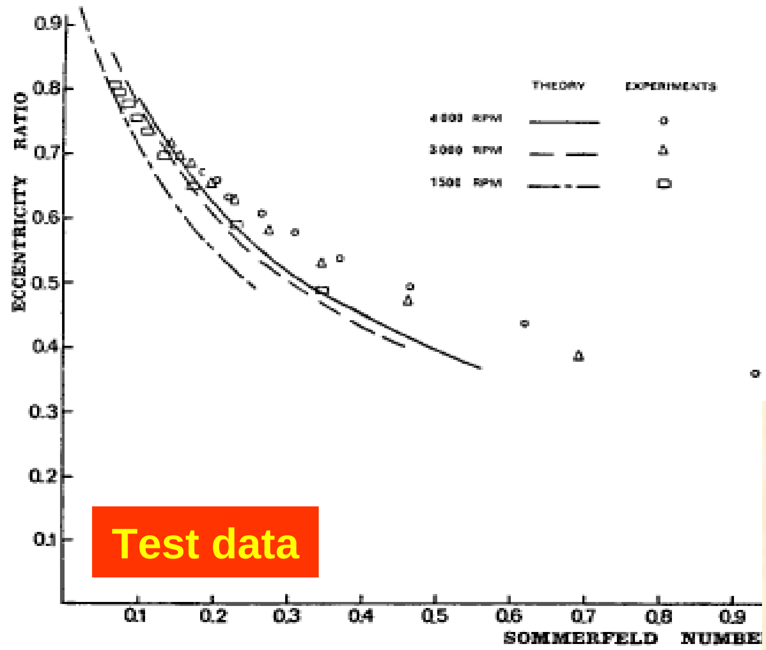

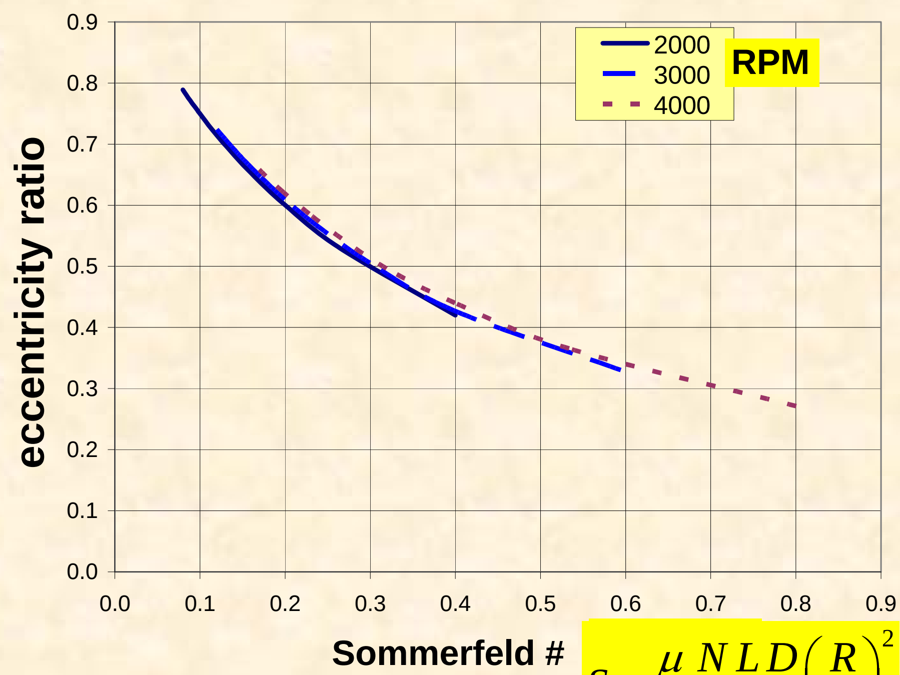

$$S = \frac{\mu \, N \, L \, D}{W} \left(\frac{R}{C} \right)^2$$

Eccentricity ratio (*e/c*) vs Sommerfeld #

Ferron et al. bearing (1983)

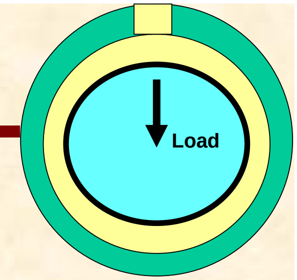

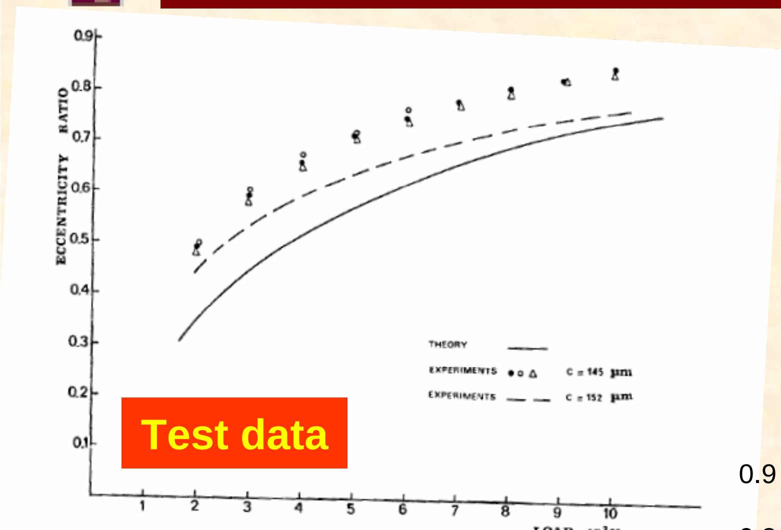

Fig. 5 Eccentricity ratio versus load at 2000 rpm

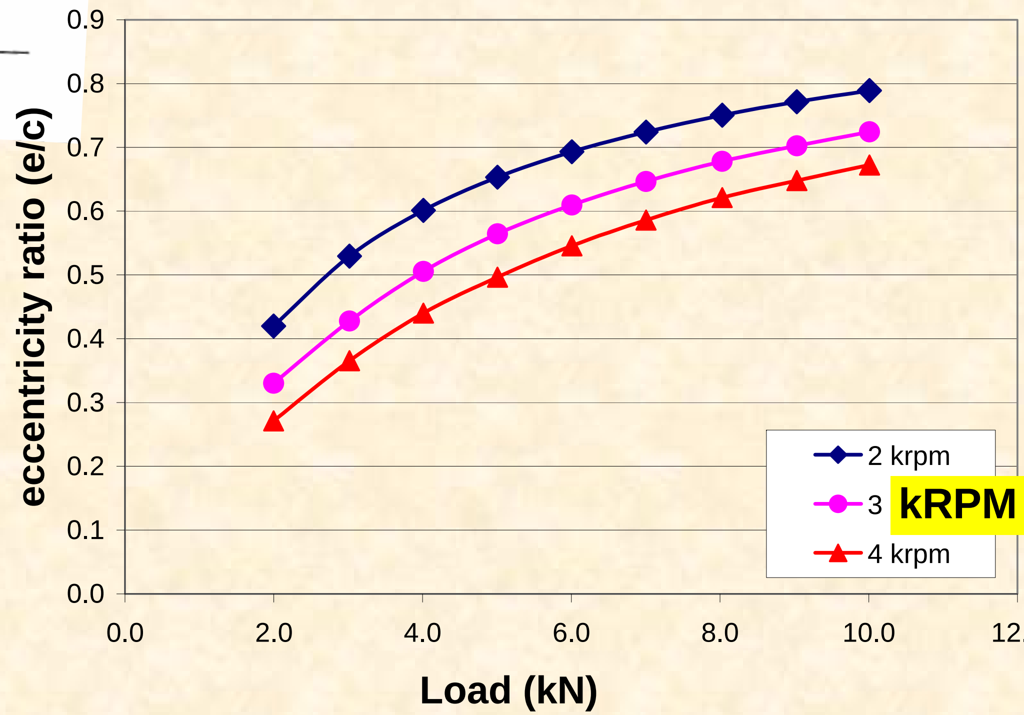

Journal eccentricity (*e/c*) vs. applied static load

Ferron et al. bearing (1983)

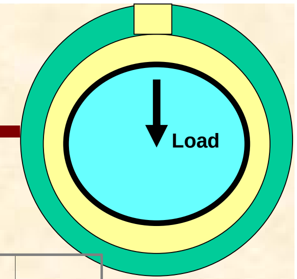

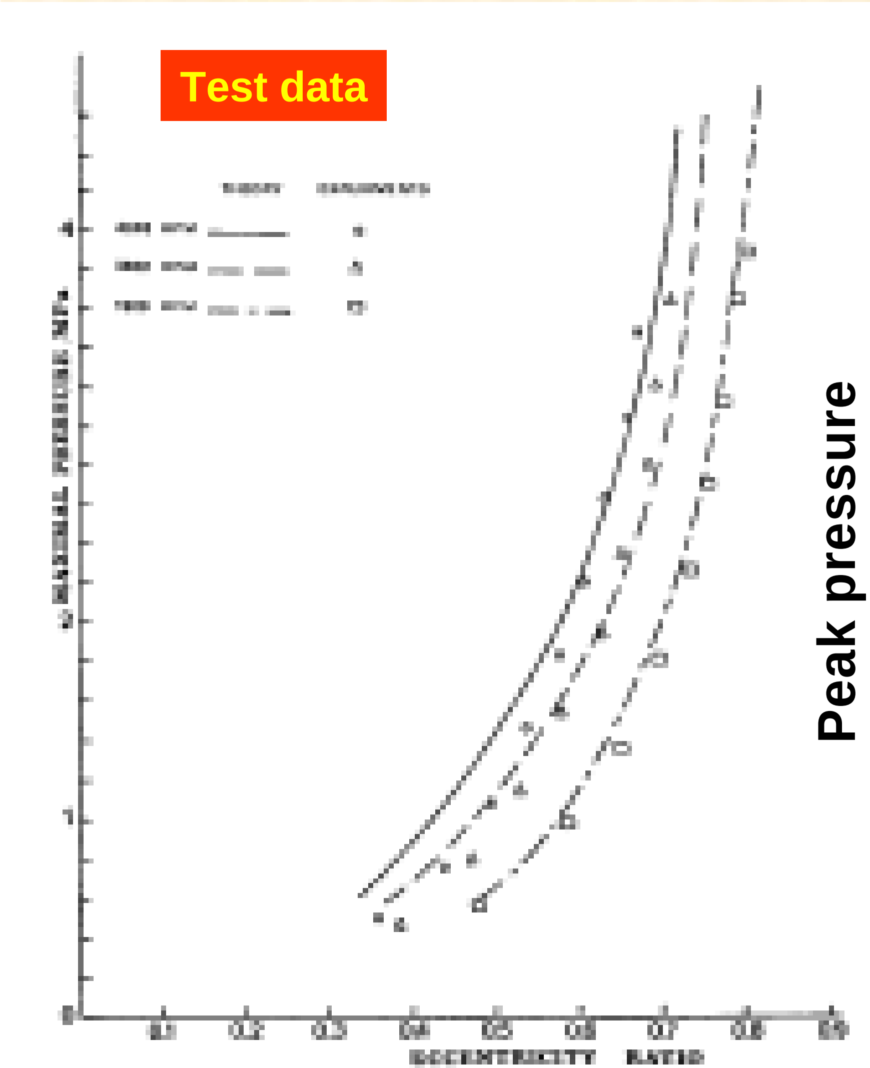

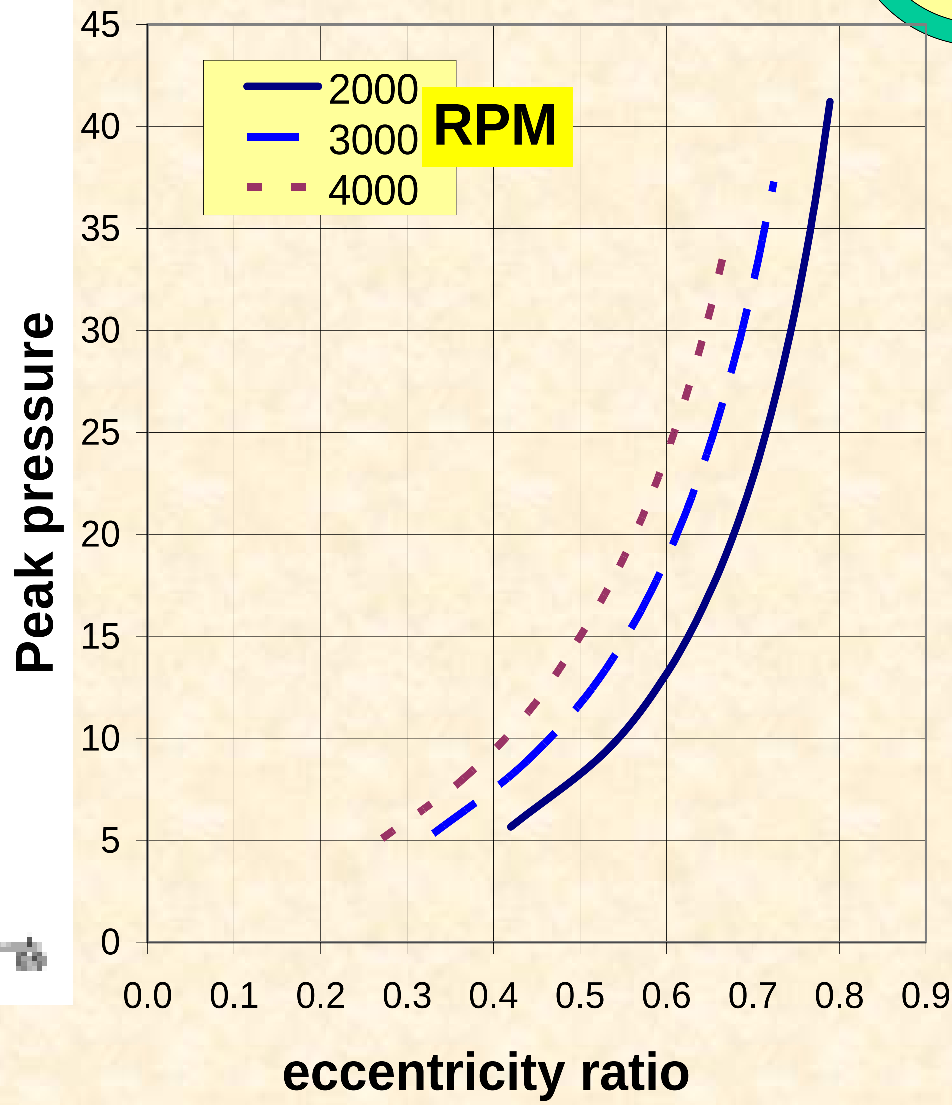

Peak film pressure vs. eccentricity ratio (*e/c*)

Ferron et al. bearing (1983)

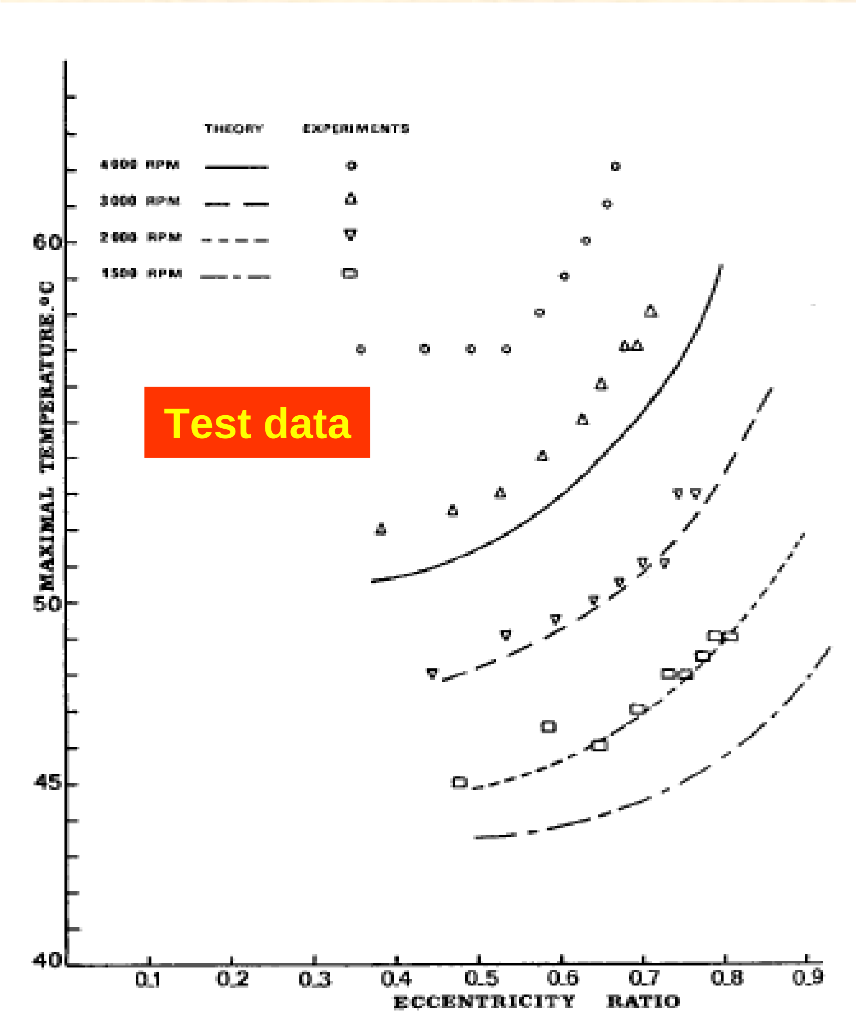

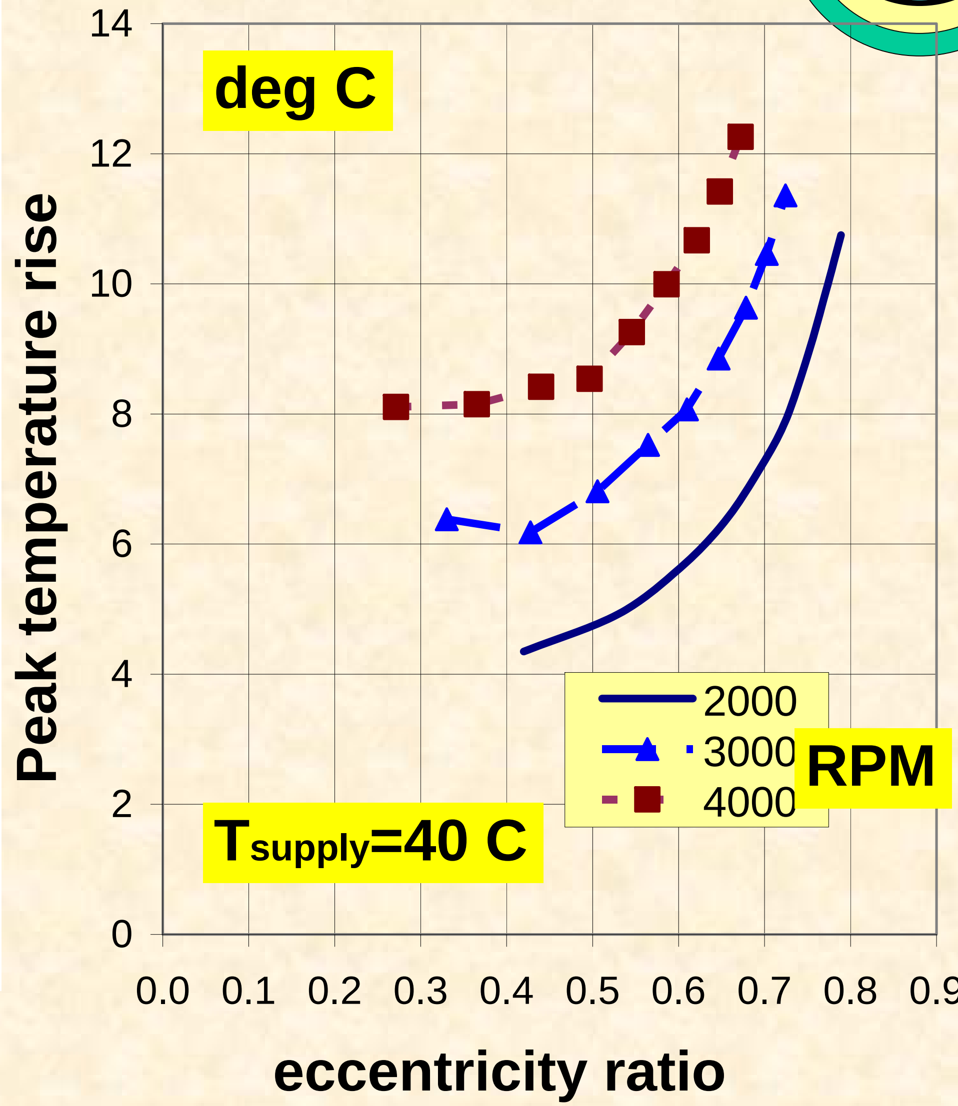

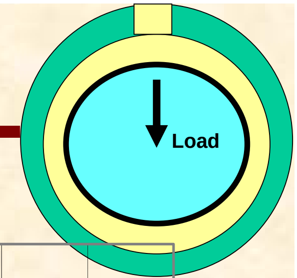

Peak film temperature vs. eccentricity ratio (*e/c*)

Example 2: two axial groove bearing

Journal diameter	D	100	mm
Bearing Length	L	80	mm
Radial clearance	c	0.085	mm
preload	r_p	0	mm
Feed groove width		70	mm
Pad arc length		162	deg
Lubricant			
Density	ρ	870	kg/m3
Specific Heat	Cp	2000	J/kg-C
Thermal conductivity	κ	0.13	W/m-C
Viscosity at 40 C	μ	0.0293	Pa.s
Visc-temp coefficient	α	0.032	1/C
Inlet oil temperature		35,40,50	C
Inlet oil pressure		0.7,1.4, 2.1	bar
Load range		1kN-10 kN	
Speed range		1-4 kRPM	
Prandtl No		451	

Brito,F.P., Miranda, A.S., Bouter, J., and Fillon, M., Frene, J., and R. Boncompain, 2007, "Experimental investigation on the influence of Supply temperature and Supply Pressure on the Performance of a Two-Axial Groove Hydrodynamic Journal Bearing", ASME Journal of Tribology, Vol. 129, pp. 98-105,

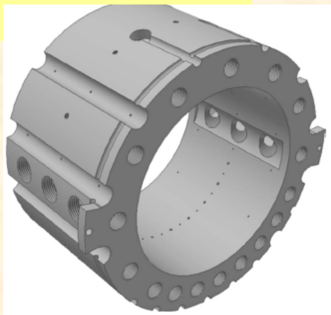

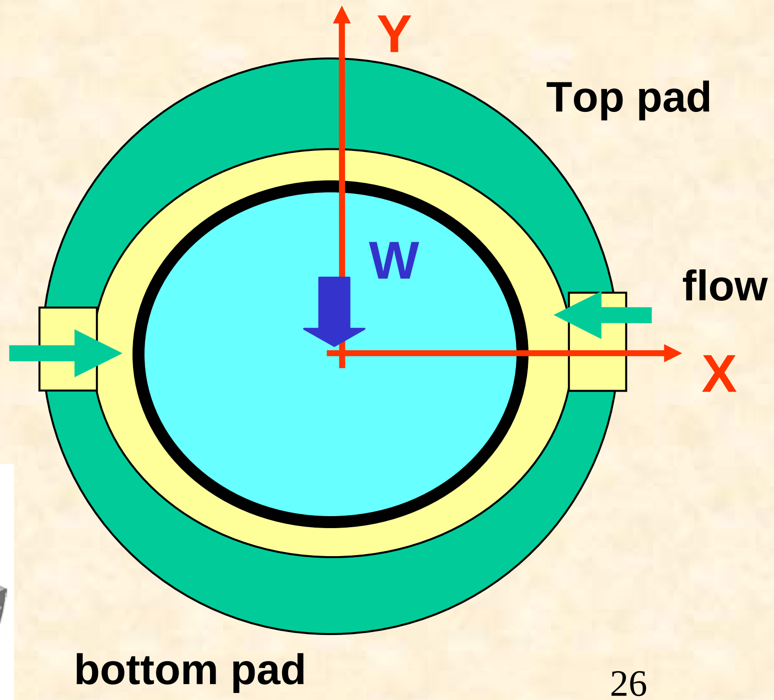

Brito et al. bearing (2007)

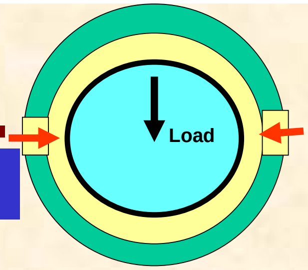

Midplane pressure | **Film temperature** | **Journal locus**

Test data

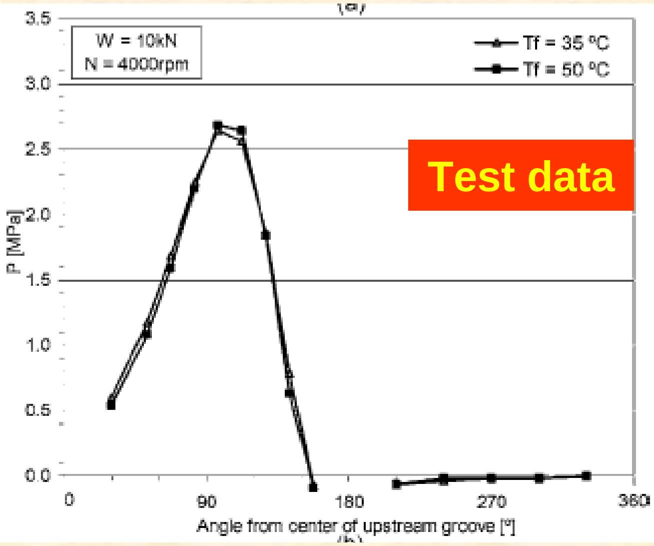

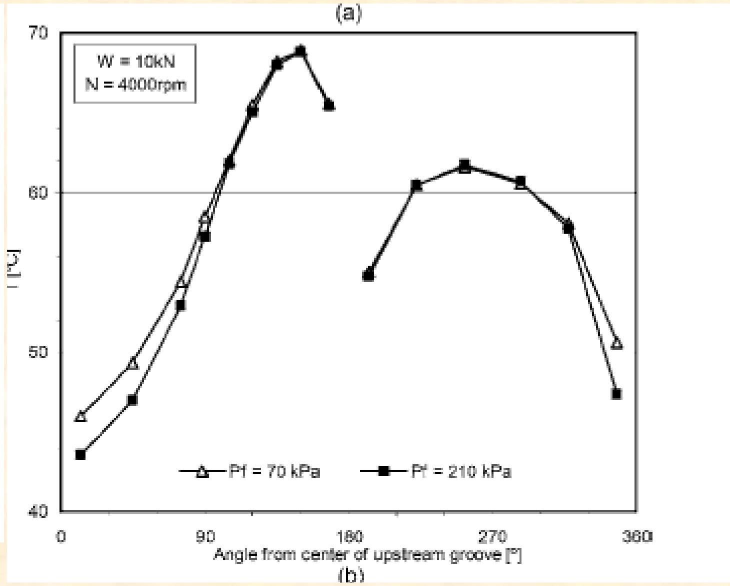

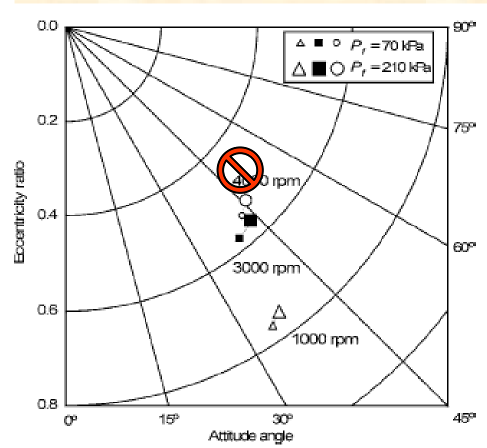

Predictions

e/c=0.43

ϕ = 56 deg

1.35 kW

3.0 LPM

28 bar max

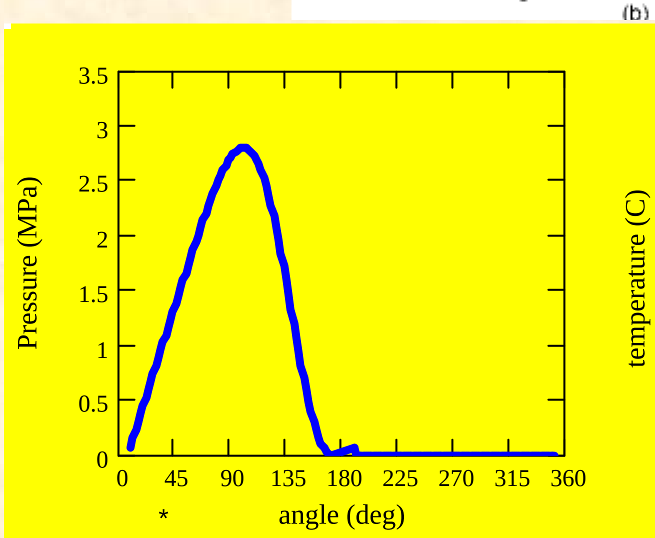

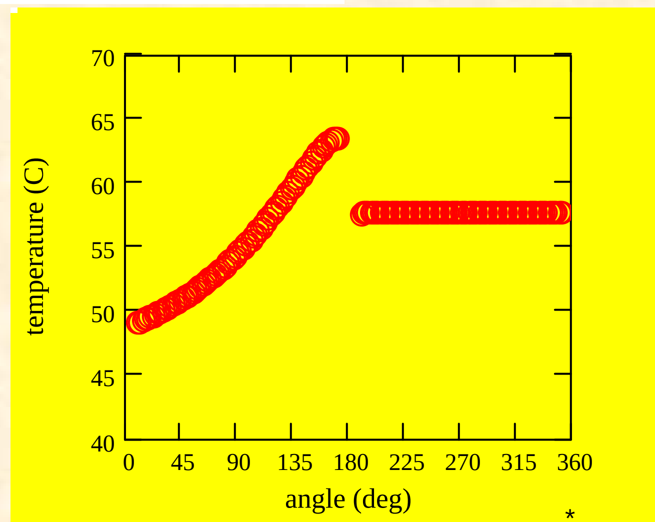

Pressure and temperature fields – 4 kRPM, 10 kN

Example 3 – Pressure dam bearing

Journal diameter	D	117.1	mm
Bearing Length	L	76.2	mm
Radial clearance	c	**0.142**	mm
pad arc		**170**	deg
Dam arc length	Θ_D	130	deg
width (0.75 L)	L_D	57.1	mm
depth		**0.4**	**mm**
Reilef groove width	L_R	19.05	mm
depth		**0.1**	**mm**
Lubricant	**ISO VG 32**		
Density	ρ	860	kg/m3
Specific Heat	Cp	2000	J/kg-C
Thermal conductivity	κ	0.13	W/m-C
Viscosity at 45 C	μ	0.028	Pa.s
Visc-temp coefficient	α	0.034	1/C
Inlet oil temperature		**40-55 ?**	C
Inlet oil pressure		**N/A**	bar
Load range		0.1-12	kN
Speed range		4,6,8,10,12	krpm

Al-Jughaiman, and Childs, D., 2007, "Static and Dynamic Characteristics for a Pressure-Dam Bearing", ASME Paper GT2007-25577

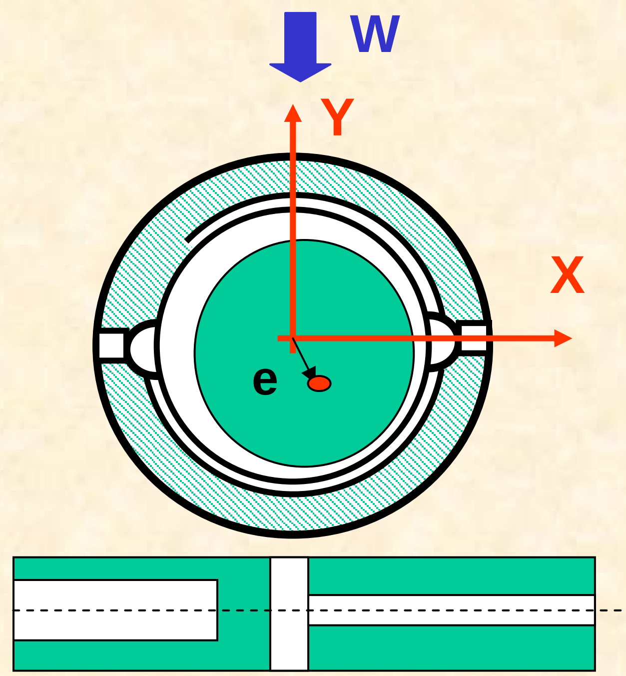

Missing details on bearing geometry, lubricant and feed conditions. Even with test data at hand, not able to reproduce test results in paper. VERY PECULIAR THERMAL EFFECTS

Example 3 – Pressure dam bearing

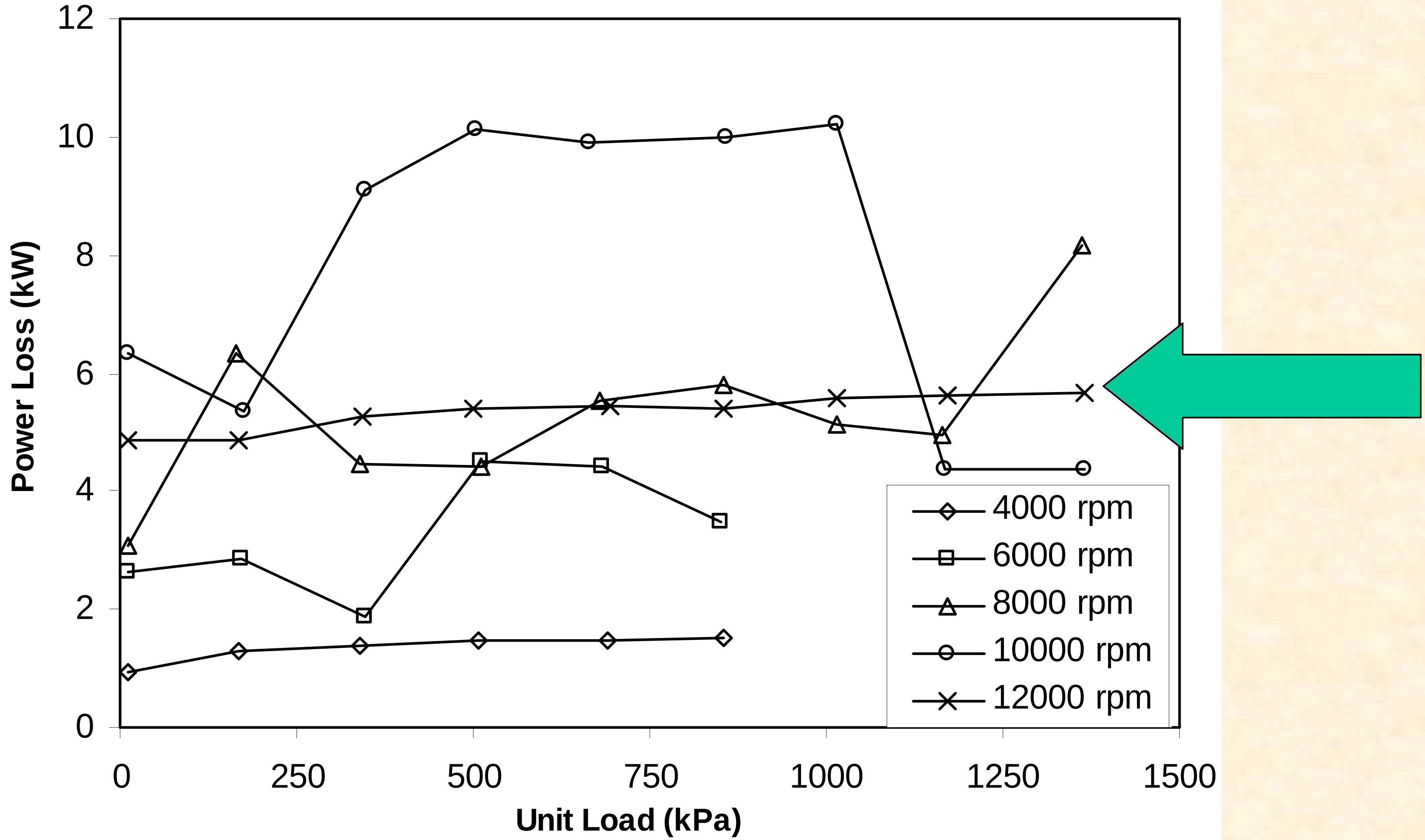

GT2007-25577 **Power loss**

Example 3 – Pressure dam bearing

TAMU Pressure Dam Bearing with relief track

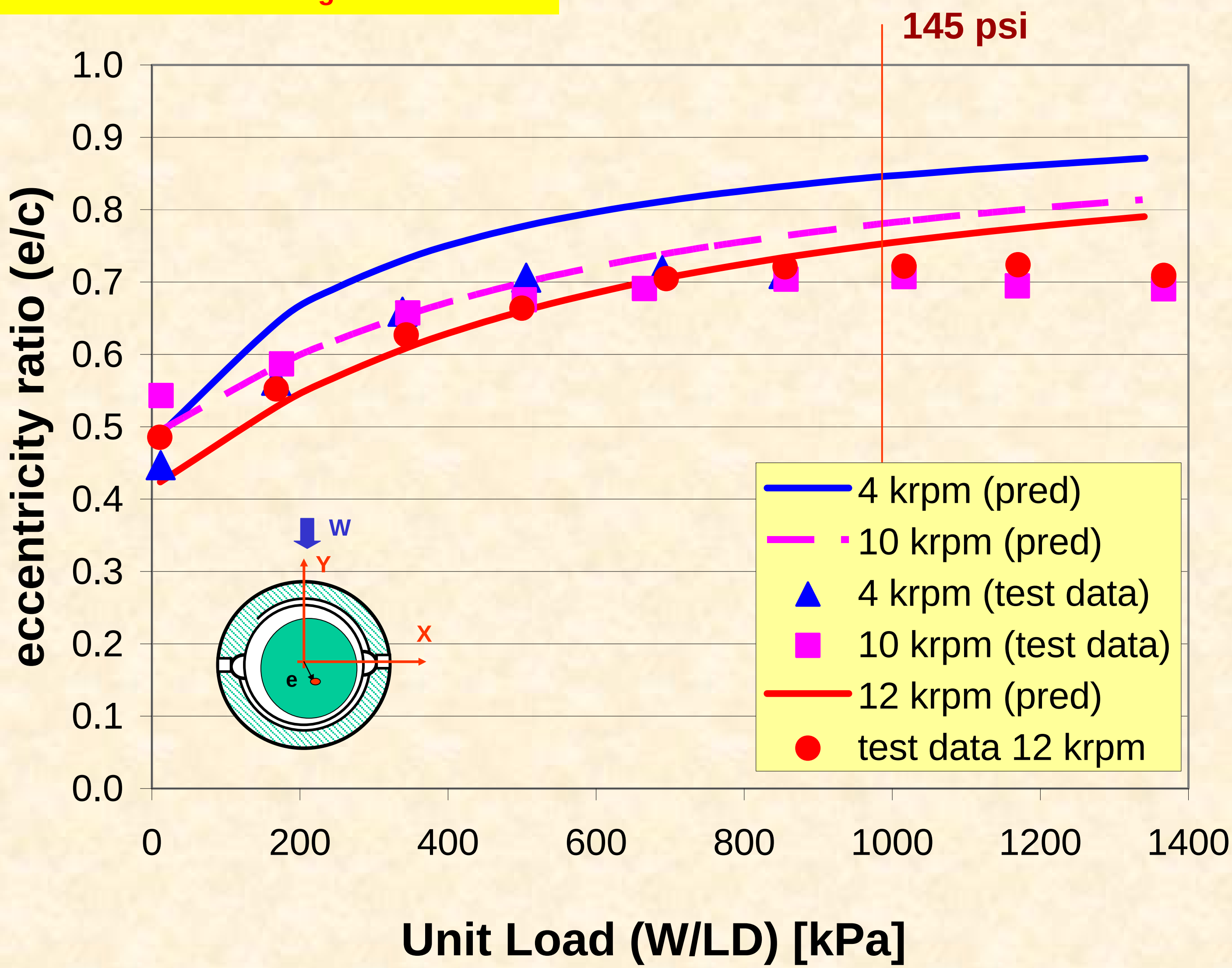

Journal eccentricity vs specific pressure

Example 3 – Pressure dam bearing

TAMU Pressure Dam Bearing

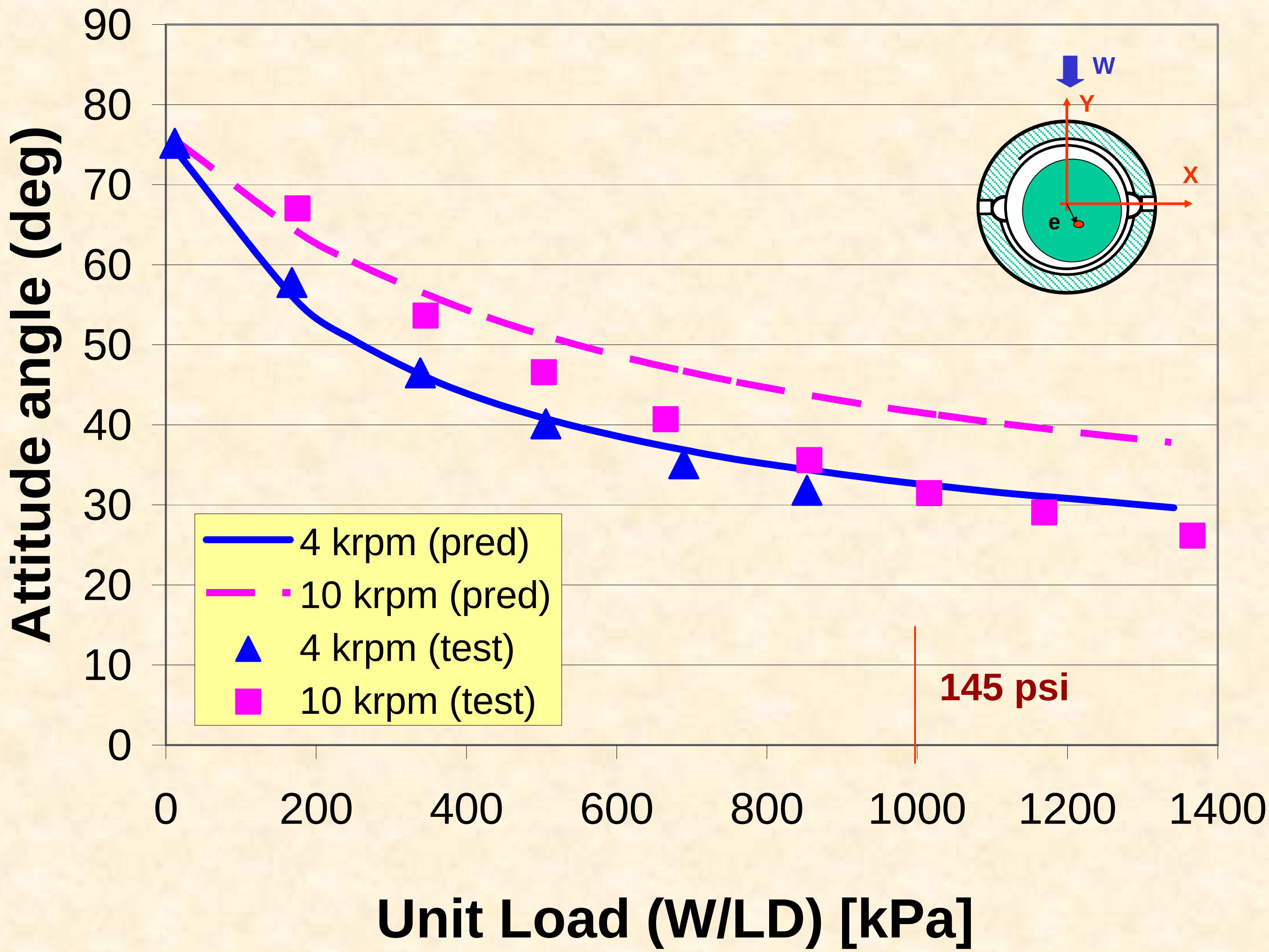

Attitude angle vs specific pressure

Example 3 – Pressure dam bearing

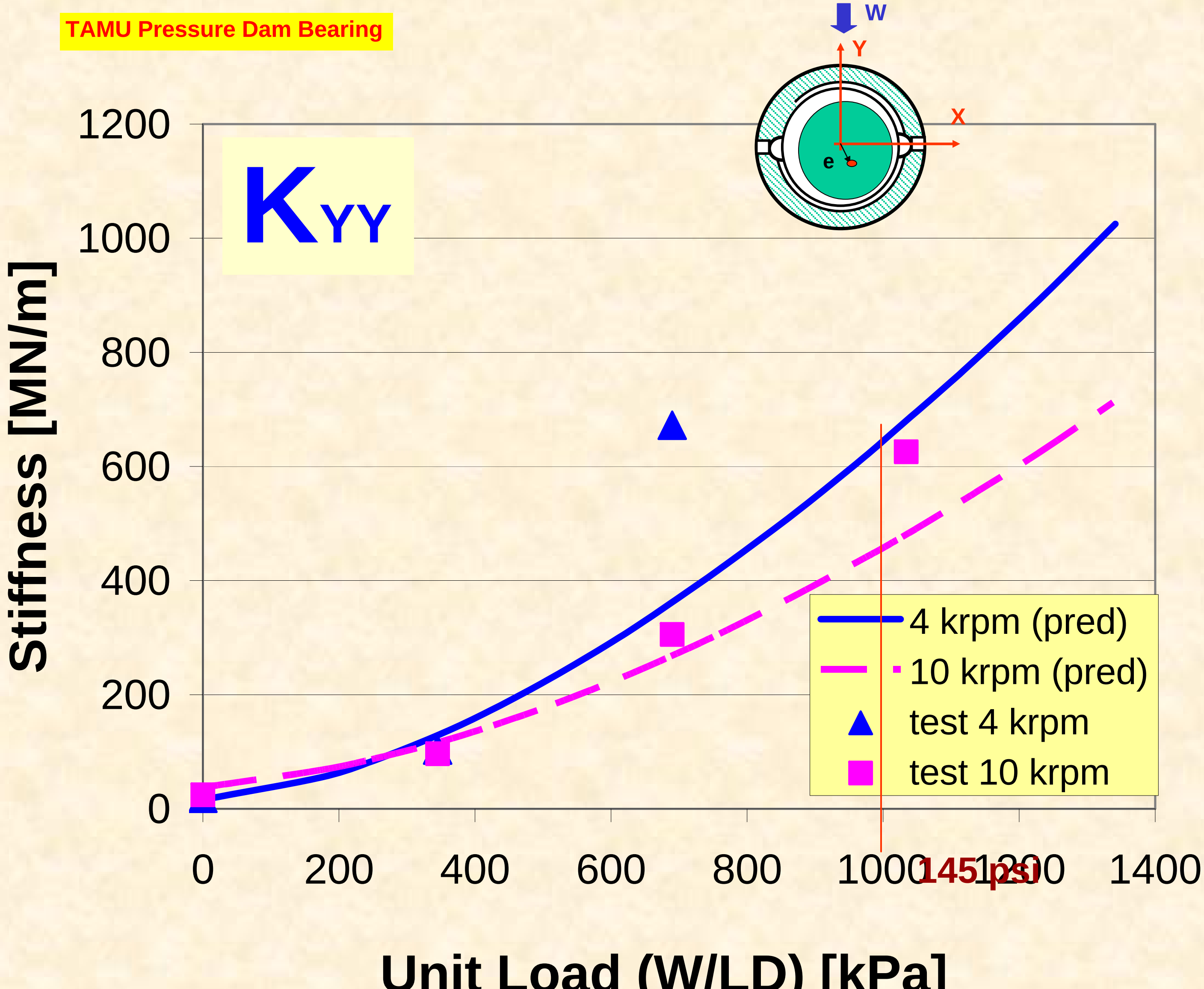

Direct stiffness K_{YY} vs specific pressure

Example 3 – Pressure dam bearing

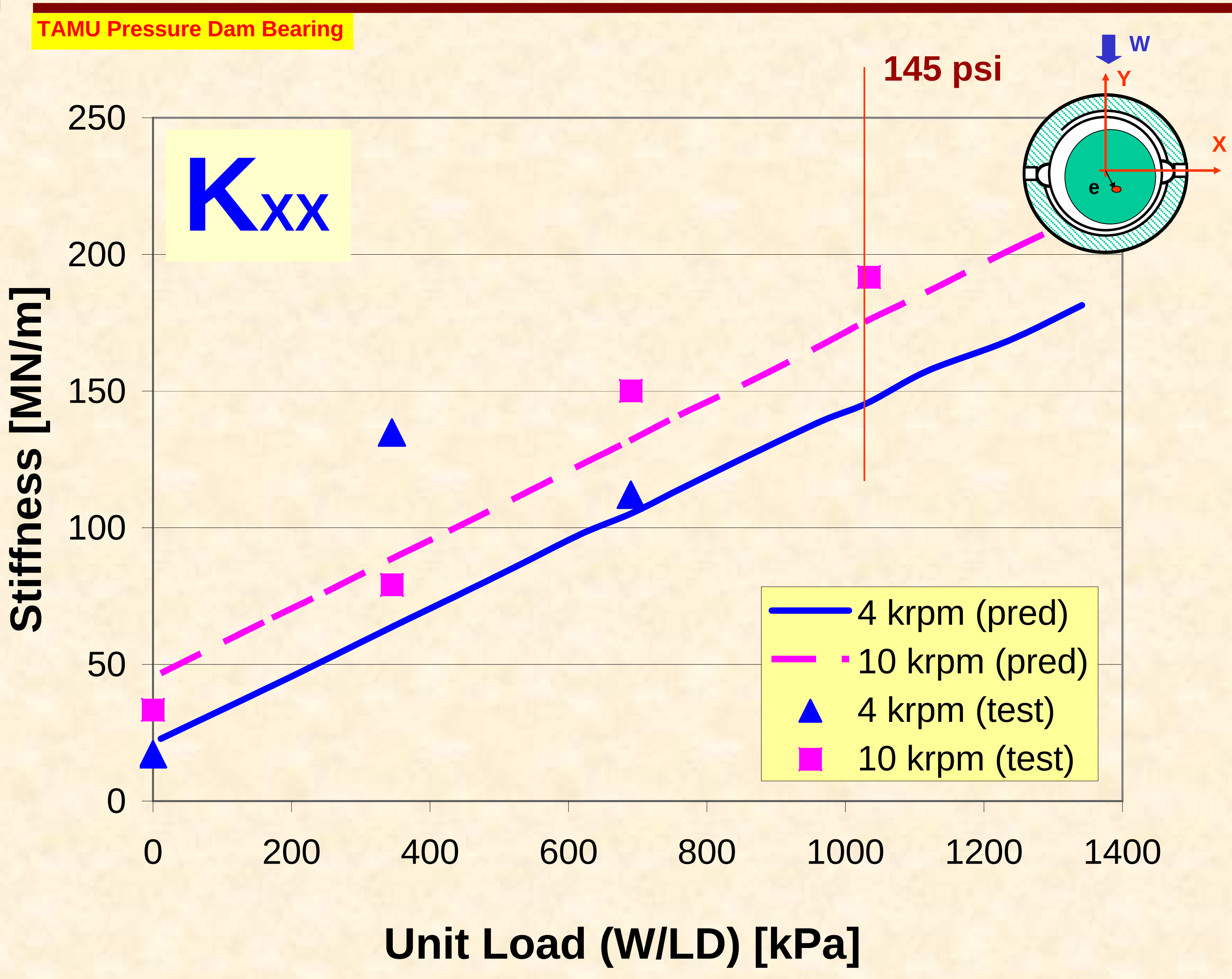

Direct stiffness K_{xx} vs specific pressure

Example 3 – Pressure dam bearing

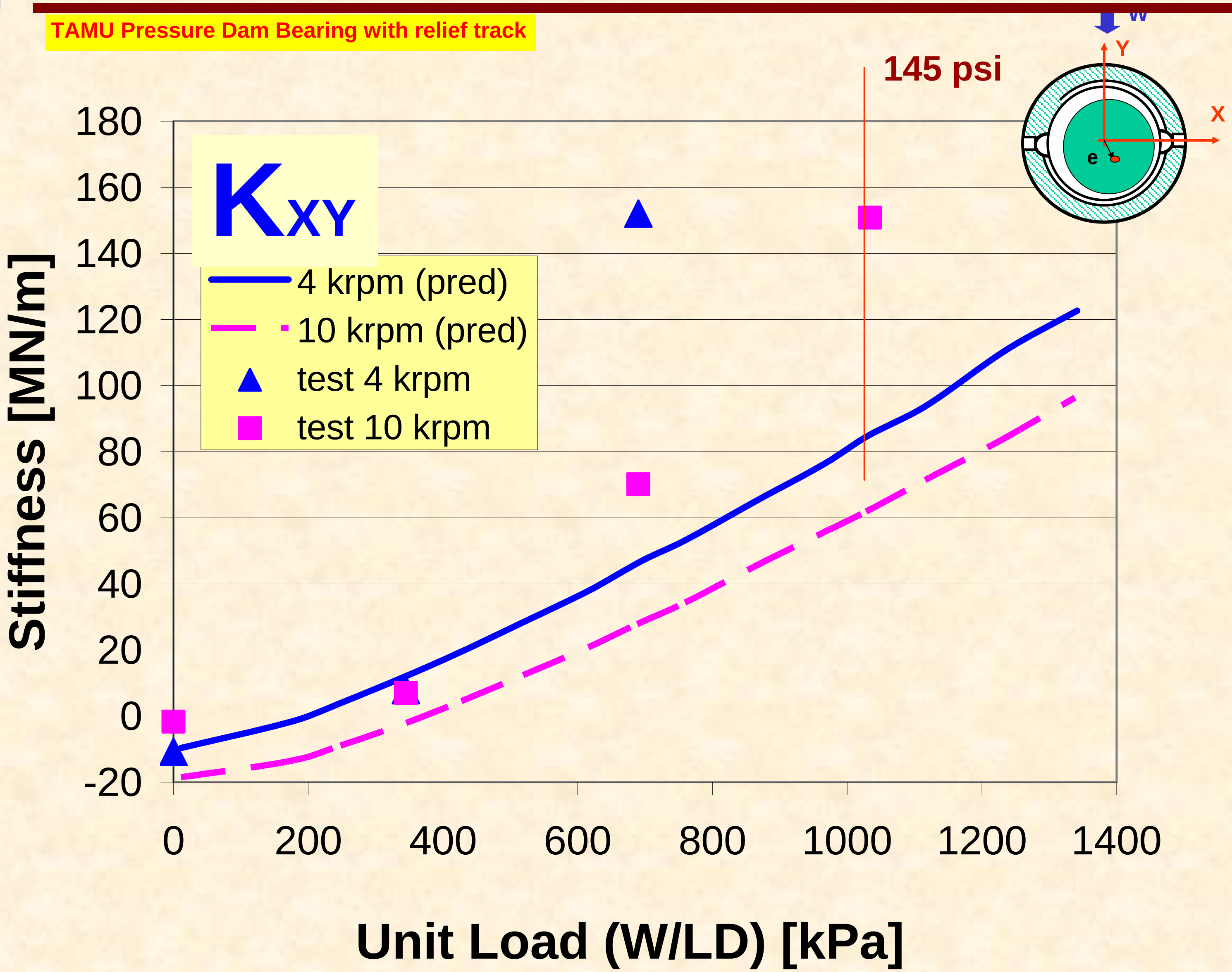

Cross stiffness K_{XY} vs specific pressure

Example 3 – Pressure dam bearing

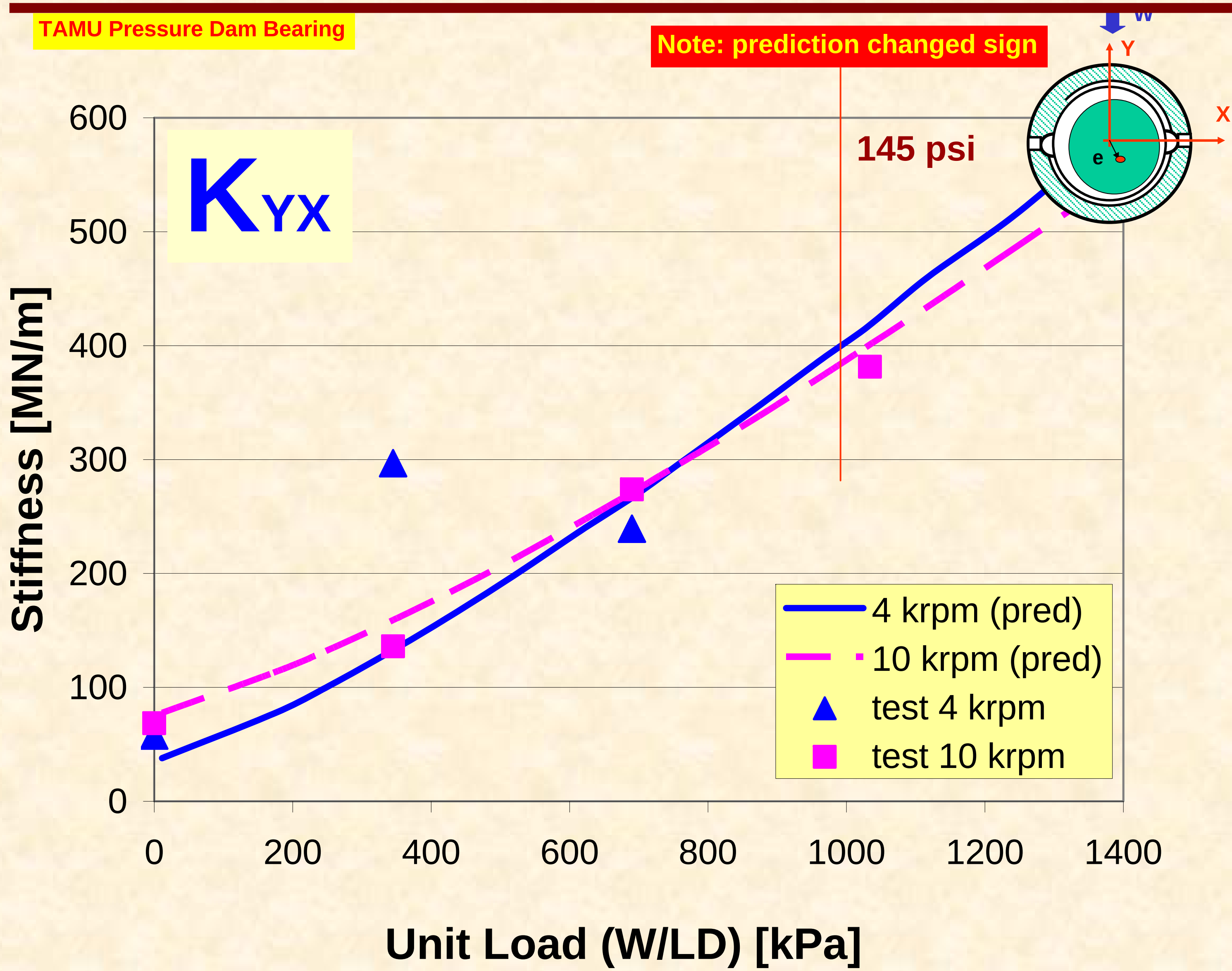

Cross stiffness K_{YX} vs specific pressure

Example 3 – Pressure dam bearing

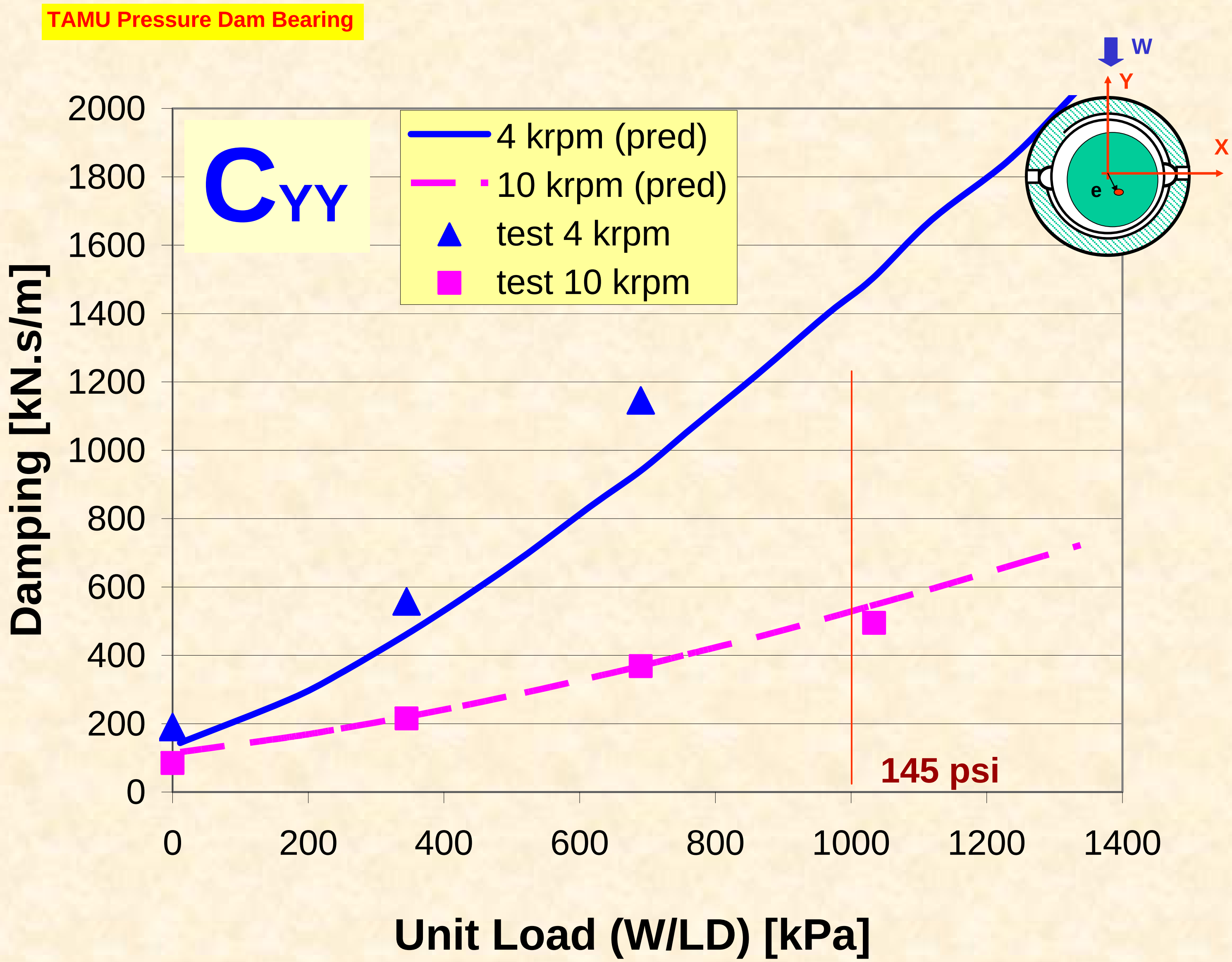

Direct DAMPING C_{YY} vs specific pressure

Example 3 – Pressure dam bearing

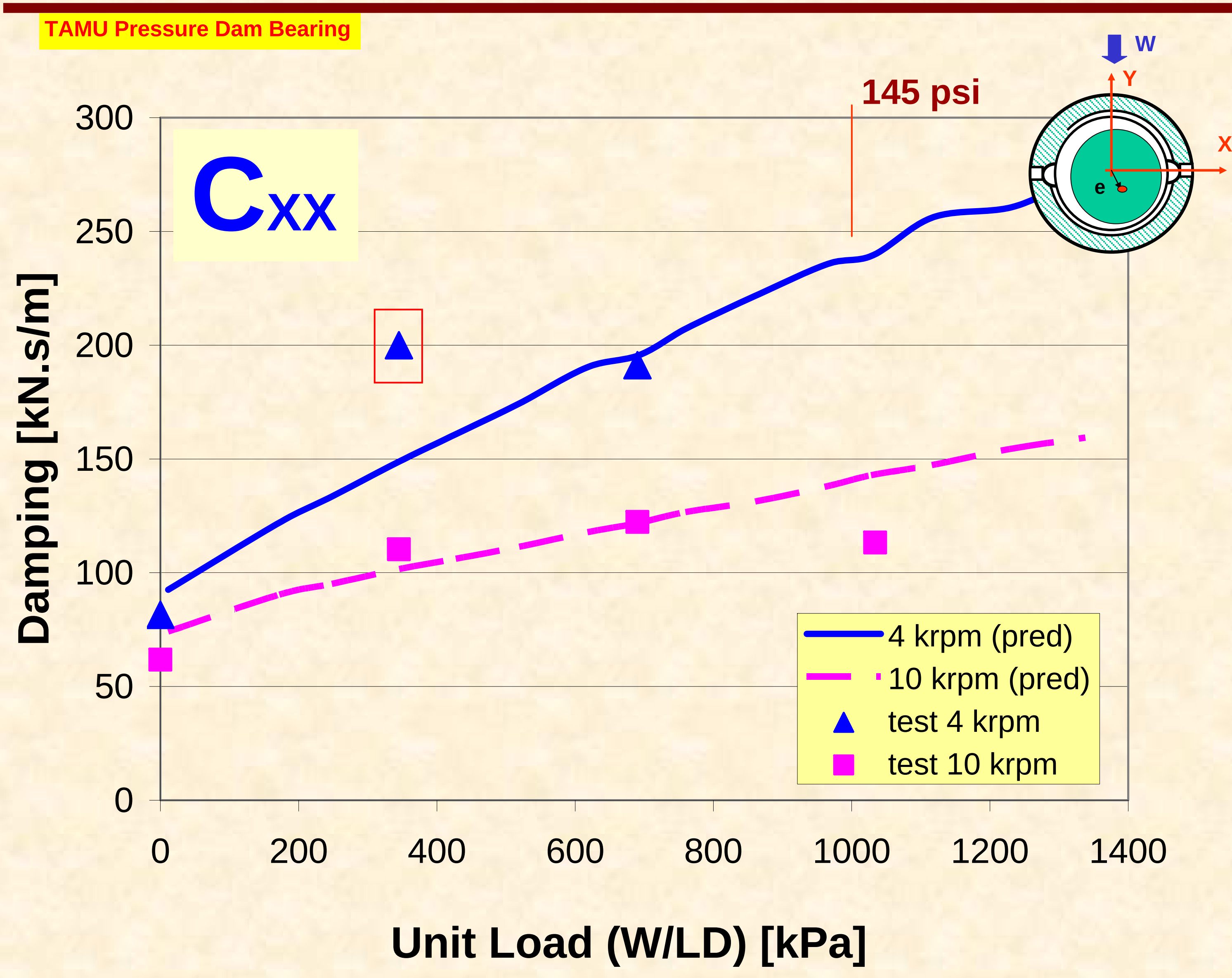

Direct DAMPING C_{XX} vs specific pressure

Example 3 – Pressure dam bearing

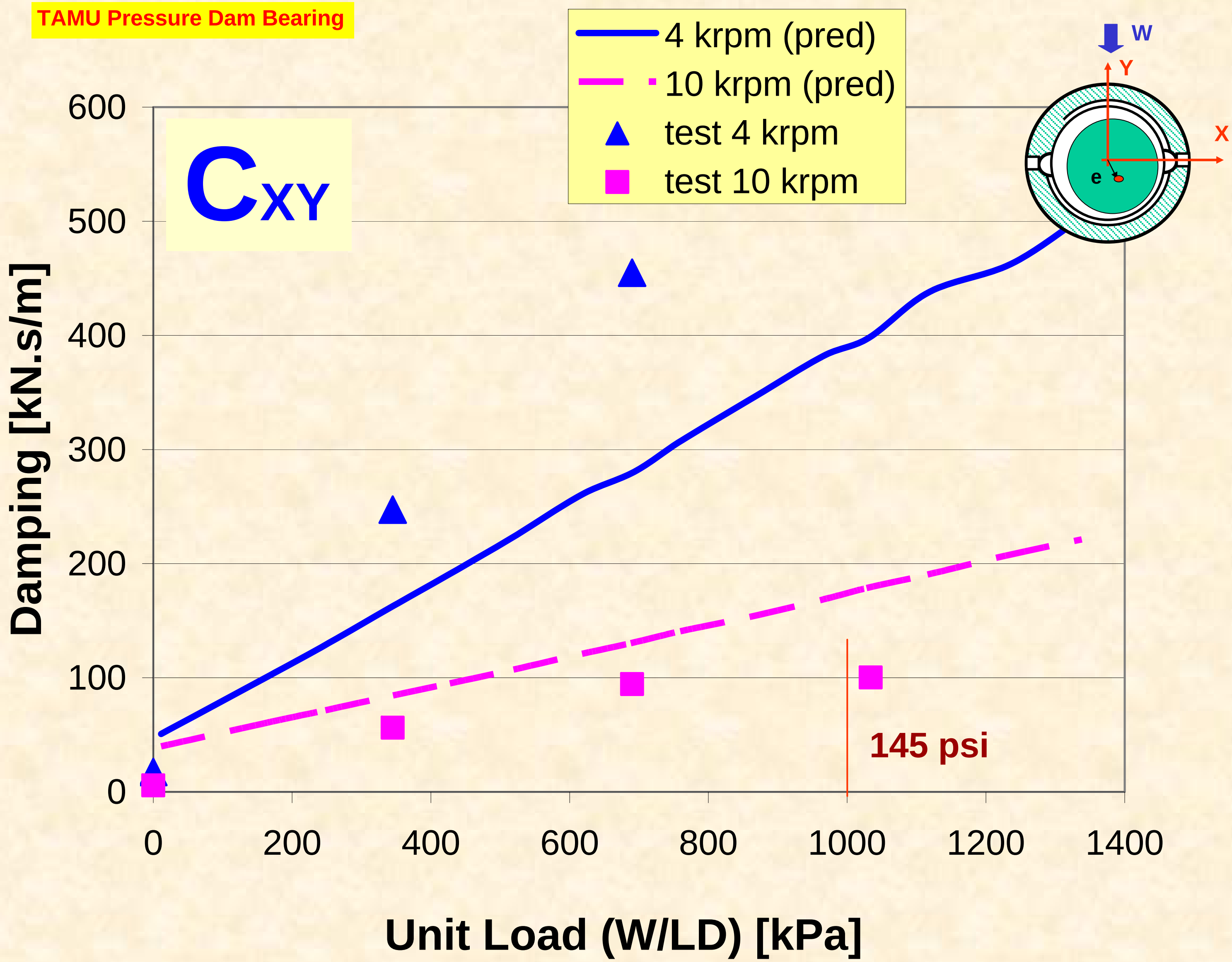

Cross DAMPING C_{XY} vs specific pressure

Example 3 – Pressure dam bearing

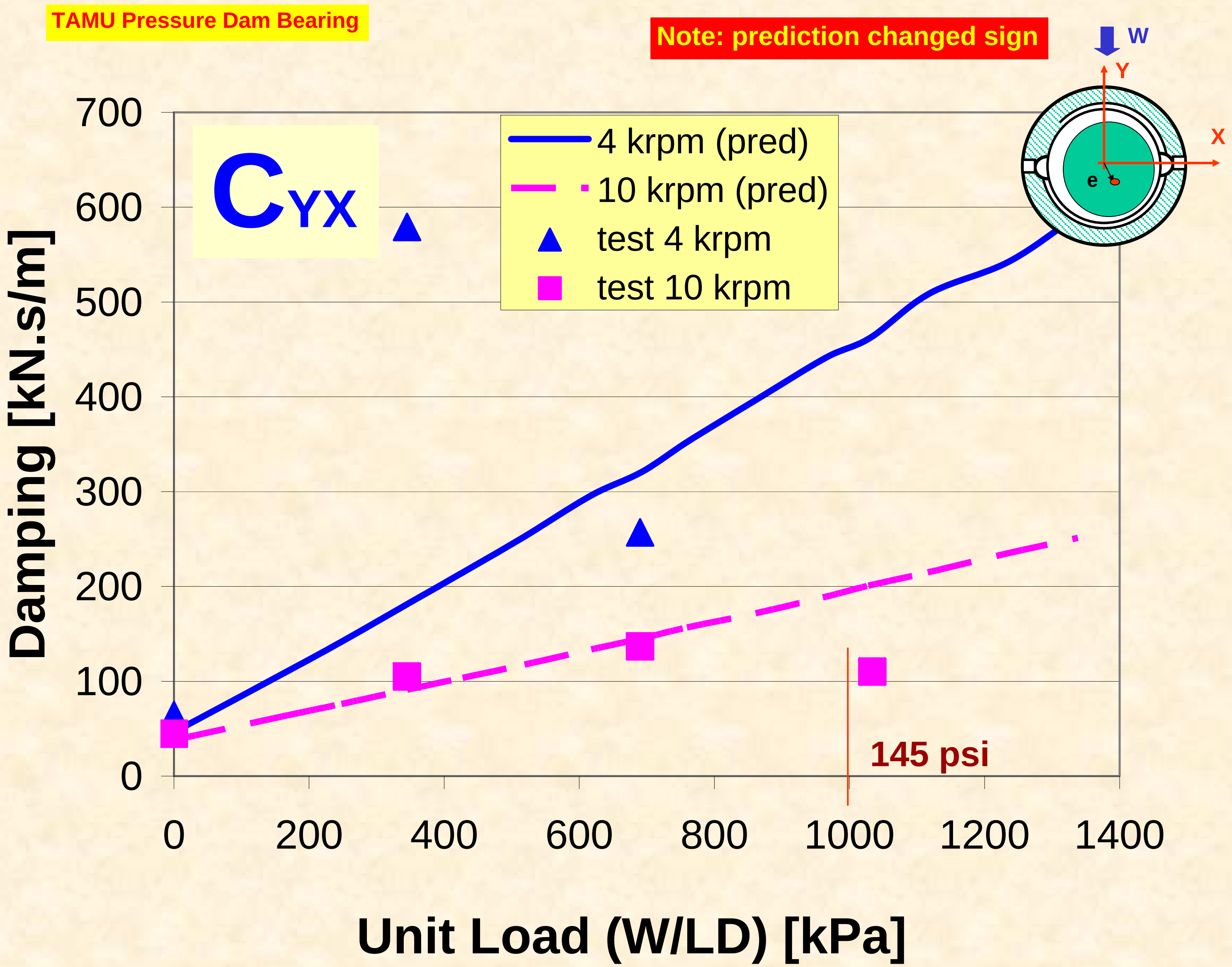

Cross DAMPING C_{YX} vs specific pressure

Example 3 – Pressure dam bearing

TAMU Pressure Dam Bearing

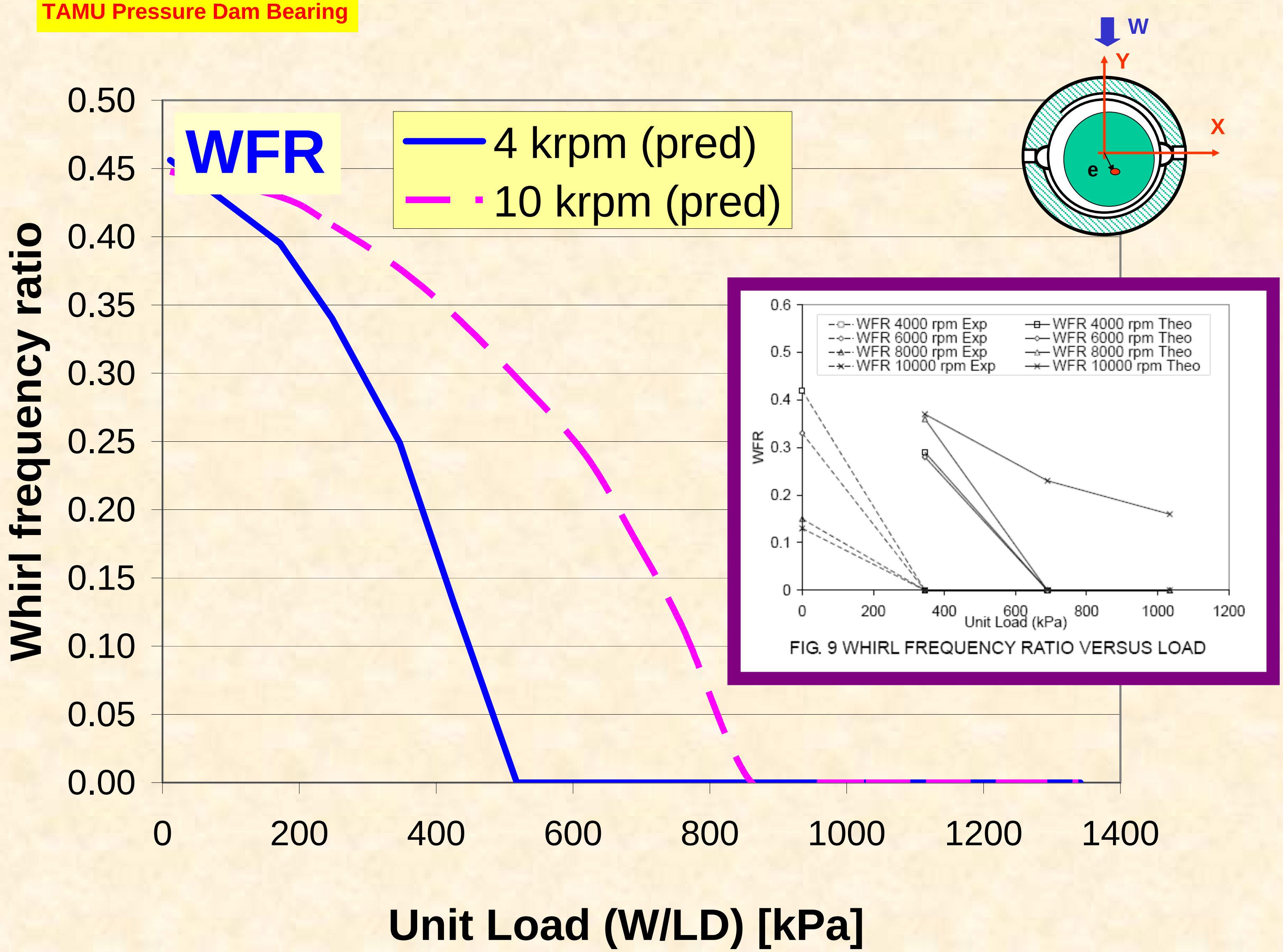

Whirl frequency ratio WFR vs specific pressure

Example 3 – Pressure dam bearing

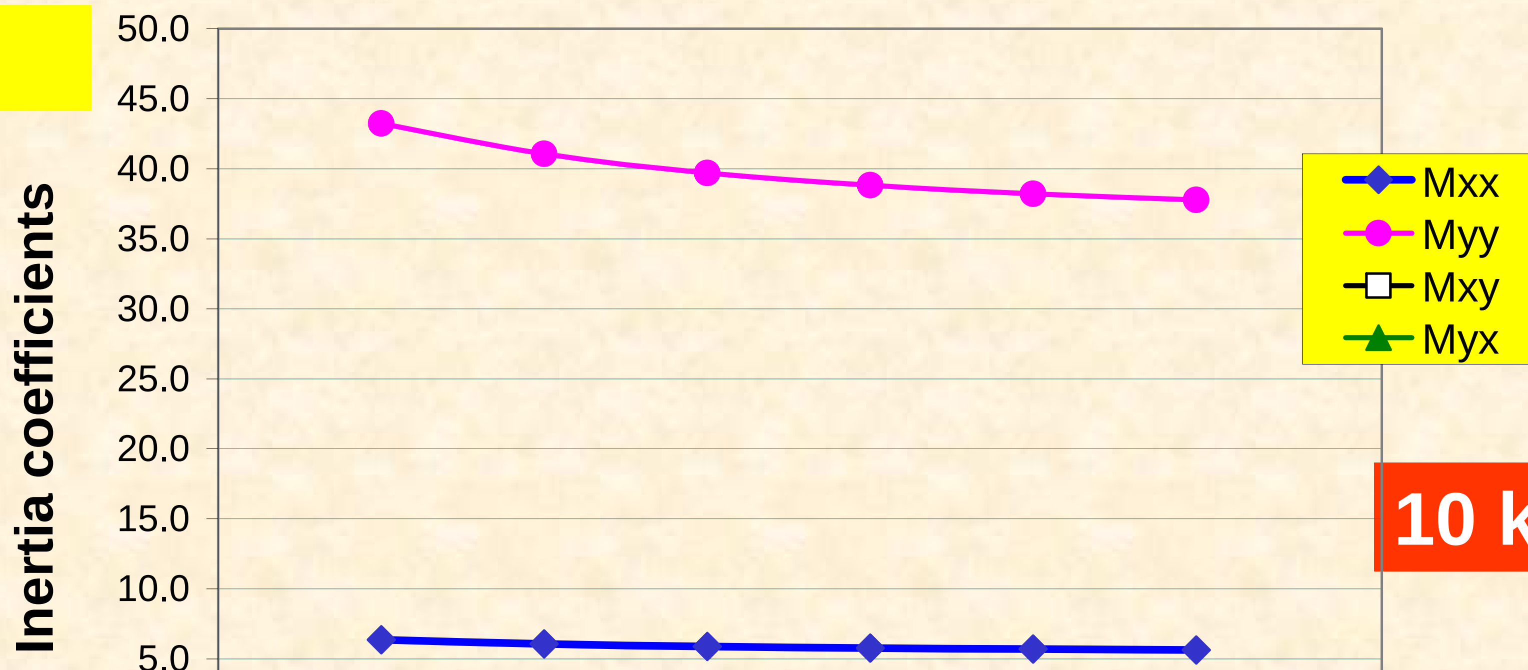

10 krpm

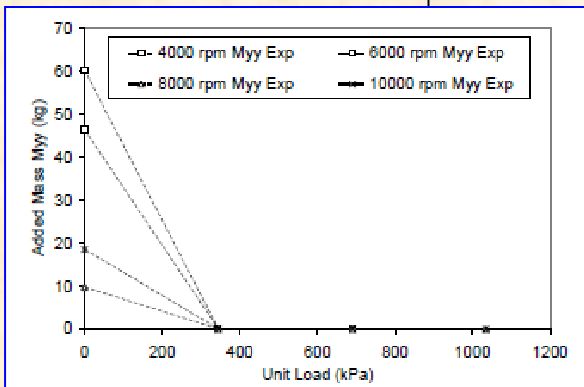

FIG. 8 (A) ADDED MASS COEFFICIENTS VERSUS LOAD

Added Mass Coefficients WFR vs specific pressure